

¹
² Susceptible host dynamics explain pathogen resilience to
³ perturbations

⁴
⁵ Sang Woo Park, . . . , Sarah Cobey

⁶ Abstract

⁷ Major priority for epidemiological research in the time of anthropogenic change is
⁸ understanding how infectious disease dynamics respond to perturbations. Interven-
⁹ tions to slow the spread of SARS-CoV-2 significantly disrupted the transmission
¹⁰ of other human pathogens. As interventions lifted, whether and when respiratory
¹¹ pathogens would eventually return to their pre-pandemic dynamics remains to be
¹² answered. To address this gap, we develop a framework for estimating pathogen re-
¹³ silience based on how fast epidemic patterns return to their pre-pandemic, endemic
¹⁴ dynamics. Our analysis suggests that some pathogens may have settled to endemic
¹⁵ cycles that are different from their pre-pandemic patterns. Finally, we show that
¹⁶ the replenishment rate of the susceptible pool is a key determinant of pathogen re-
¹⁷ silience. Our framework offers a novel perspective to characterizing the dynamics of
¹⁸ endemic pathogens and their responses to SARS-CoV-2 interventions. [SWP: Need
¹⁹ to emphasize broader implications.]

Non-pharmaceutical interventions (NPIs) to slow the spread of SARS-CoV-2 disrupted the transmission of other human respiratory pathogens, adding uncertainties to their future epidemic dynamics and the overall public health burden [1]. As interventions lifted, large heterogeneities in outbreak dynamics were observed across different pathogens in different countries, with some pathogens exhibiting earlier resurgences than others [2, 3, 4]. Heterogeneities in the overall reduction in transmission and the timing of re-emergence likely reflect differences in NPI patterns, pathogen characteristics, immigration/importation from other countries, and pre-pandemic pathogen dynamics [5]. Therefore, comparing the differential impact of the pandemic NPIs across pathogens can provide unique opportunities to learn about underlying pathogen characteristics, such as their transmissibility or duration of immunity, from heterogeneities in re-emergence patterns [6].

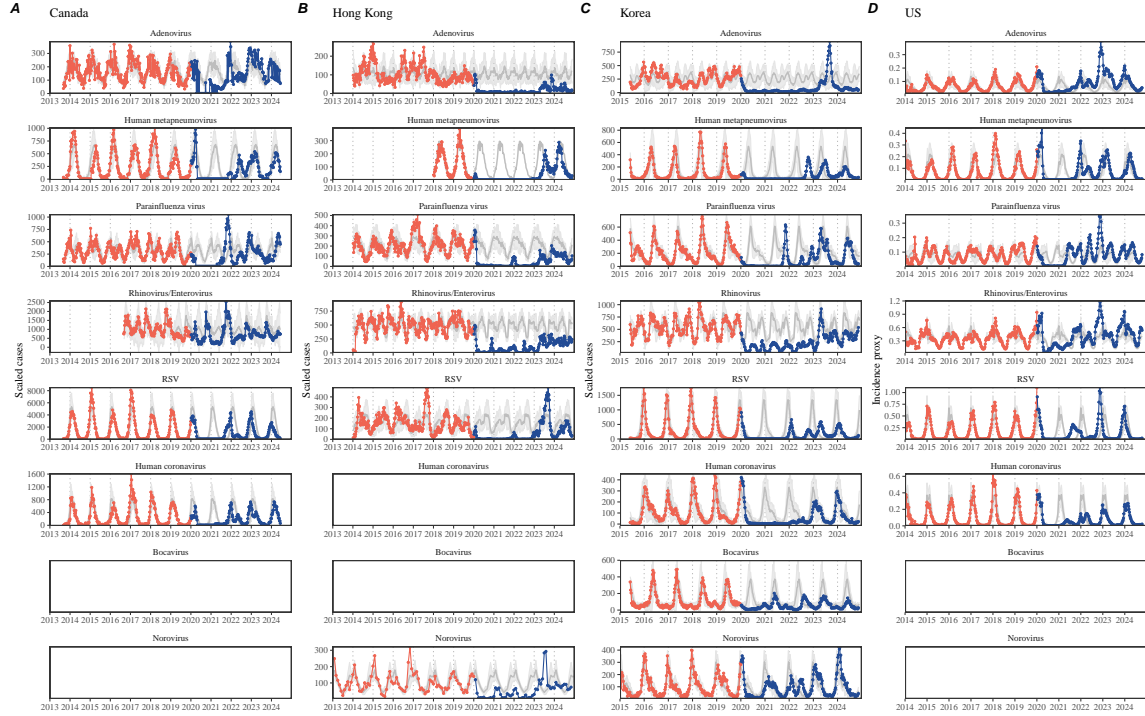


Figure 1: Observed heterogeneity in responses to COVID-19 pandemic across respiratory pathogens and norovirus in (A) Canada, (B) Hong Kong, (C) Korea, and (D) US. Red points and lines represent data before 2020. Blue points and lines represent data since 2020. Gray lines and shaded regions represent the mean seasonal patterns and corresponding 95% confidence intervals around the mean. Mean seasonal patterns were calculated by aggregating cases before 2020 into 52 weekly bins and taking the average in each week. Cases were scaled to account for changes in testing patterns (Materials and Methods).

Even though more than five years have passed since the emergence of SARS-CoV-2, we still observe persistent changes in pathogen dynamics following the pandemic

34 NPIs: for example, compared to pre-pandemic, seasonal patterns, human metapneumovirus and bocavirus in Korea are circulating at lower levels, whereas RSV in Korea
35 seem to exhibit different seasonality (Figure 1). These observations suggest a possibility
36 for a fundamental change in pathogen dynamics following the pandemic NPIs,
37 which can be driven by permanent shift in either human behavior or population-level
38 immunity [7, 8]. Moreover, the possibility of a long-lasting impact of the pandemic
39 NPIs pose an important question for future infectious disease dynamics: can we pre-
40 dict whether and when other respiratory pathogens will eventually return to their
41 pre-pandemic dynamics?

42 So far, the majority of epidemiological analyses of respiratory pathogens in the
43 context of the pandemic NPIs have focused on characterizing the timing of rebound
44 [1, 9, 5]. Instead, we seek to characterize how fast a pathogen returns to its pre-
45 pandemic dynamics. These two concepts have subtle but important differences: for
46 example, it took more than 3 years for human metapneumovirus to rebound in Hong
47 Kong but the observed epidemic patterns in 2024 are similar to pre-pandemic seasonal
48 means, suggesting a rapid return to pre-pandemic dynamics following a perturbation
49 (Figure 1). Measuring this rate of return is particularly useful because it allows us
50 to quantify the ecological resilience of a host-pathogen system [10, 11, 12, 13].

51 In this study, we lay out theoretical and statistical approaches to characterizing
52 the resilience of a host-pathogen system based on how fast the system recovers from
53 perturbation. We begin by laying out a few representative scenarios that capture
54 the potential impact of COVID-19 interventions on endemic pathogen dynamics and
55 illustrate how resilience can be measured by comparing the pre- and post-pandemic
56 dynamics of susceptible and infected hosts. In practice, information on susceptible
57 hosts is often unavailable, making this theoretical approach infeasible. Instead, we
58 utilize a mathematical technique to reconstruct empirical attractors from the data
59 [14], which allows us to measure the rate at which the host-pathogen system ap-
60 proaches this empirical attractor after a perturbation; this rate corresponds to the
61 resilience of the host-pathogen system. We use this method to analyze pathogen
62 surveillance data for respiratory and non-respiratory pathogens from Canada, Hong
63 Kong, Korea, and US. Finally, we show that susceptible host dynamics explain vari-
64 ation in pathogen resilience.

66 Conceptual introduction to pathogen resilience

67 In classical ecological literature, resilience of an ecological system is measured by
68 the rate at which the system returns to its reference state following a perturbation
69 [10, 11, 12, 13]. This rate corresponds to the largest real part of the eigenvalues of
70 the linearized system near equilibrium—here, we refer to this value as the *intrinsic*
71 resilience of the system, which represents the expected rate of return from perturbed
72 states. However, respiratory pathogens often exhibit seasonal variation in transmis-
73 sion, meaning that the intrinsic resilience of a host-pathogen system varies across

74 season. Nonetheless, we can still measure the *empirical* resilience of a host-pathogen
75 system by looking at how fast the system returns to the pre-pandemic, endemic
76 dynamics after interventions are lifted.

77 As an example, we begin with a simple Susceptible-Infected-Recovered-Susceptible
78 (SIRS) model with seasonally forced transmission and demography (i.e., birth and
79 death). The SIRS model is the simplest model that allows for waning of immunity
80 and is commonly used for modeling the dynamics of respiratory pathogens [15]. First,
81 consider an intervention that reduce transmission by 50% for 6 months starting in
82 2020, which causes epidemic patterns to deviate from its original stable annual cycle
83 for a short period of time and eventually come back (Figure 2A). To measure the
84 resilience of this system empirically, we first need to be able to measure the distance
85 from its pre-pandemic attractor. There are many ways we can measure the distance
86 from attractor, but for illustrative purposes, we choose one of the most parsimonious
87 approach: that is, we look at how the susceptible (S) and infected (I) populations
88 change over time and measure the distance on the SI phase plane (Figure 2B). In this
89 simple case, the locally estimated scatterplot smoothing (LOESS) fit indicates that
90 the distance from attractor decreases exponentially (linearly on a log scale) on aver-
91 age (Figure 2C). Furthermore, the overall rate of return approximates the intrinsic
92 resilience of the seasonally unforced system (Figure 2C).

93 Alternatively, NPIs can have a lasting impact on the pathogen dynamics; as an
94 example, we consider a scenario in which a 10% reduction in transmission persists
95 even after the NPIs are lifted (Figure 2D–F). In such cases in practice, we can-
96 not know whether the pathogen will return to its original cycle or a different cycle
97 until many years have passed, and we cannot measure the distance to the new un-
98 known attractor that the system might eventually approach. Nonetheless, we can
99 still measure the distance from the pre-pandemic attractor and ask how the distance
100 changes over time (Figure 2E). The LOESS fit suggests that the distance from the
101 pre-pandemic attractor will initially decrease exponentially on average (equivalently,
102 linearly on a log scale) and eventually plateau (Figure 2F). Here, a permanent 10%
103 reduction in transmission rate slows the system, which causes the distance from the
104 pre-pandemic attractor initially to decrease at a slower rate (Figure 2F) than it would
105 have otherwise (Figure 2C) before plateauing at a fixed distance between the two
106 attractors. This example shows that resilience is not necessarily an intrinsic prop-
107 erty of a specific pathogen. Instead, pathogen resilience is a property of a specific
108 attractor that a host-pathogen system approaches, which depends on both pathogen
109 and host characteristics.

110 Finally, transient phenomena can further complicate the picture (Figure 2G–
111 I). For example, a stage-structured model initially exhibits a stable annual cycle,
112 but perturbations from NPIs cause the epidemic to shift to biennial cycles (Figure
113 2G). The system eventually approaches the original pre-pandemic attractor (Figure
114 2H), suggesting that this biennial cycle is a transient phenomenon. The LOESS fit
115 indicates that the distance from the attractor initially decreases exponentially at a
116 rate that is consistent with the intrinsic resilience of the seasonally unforced stage-

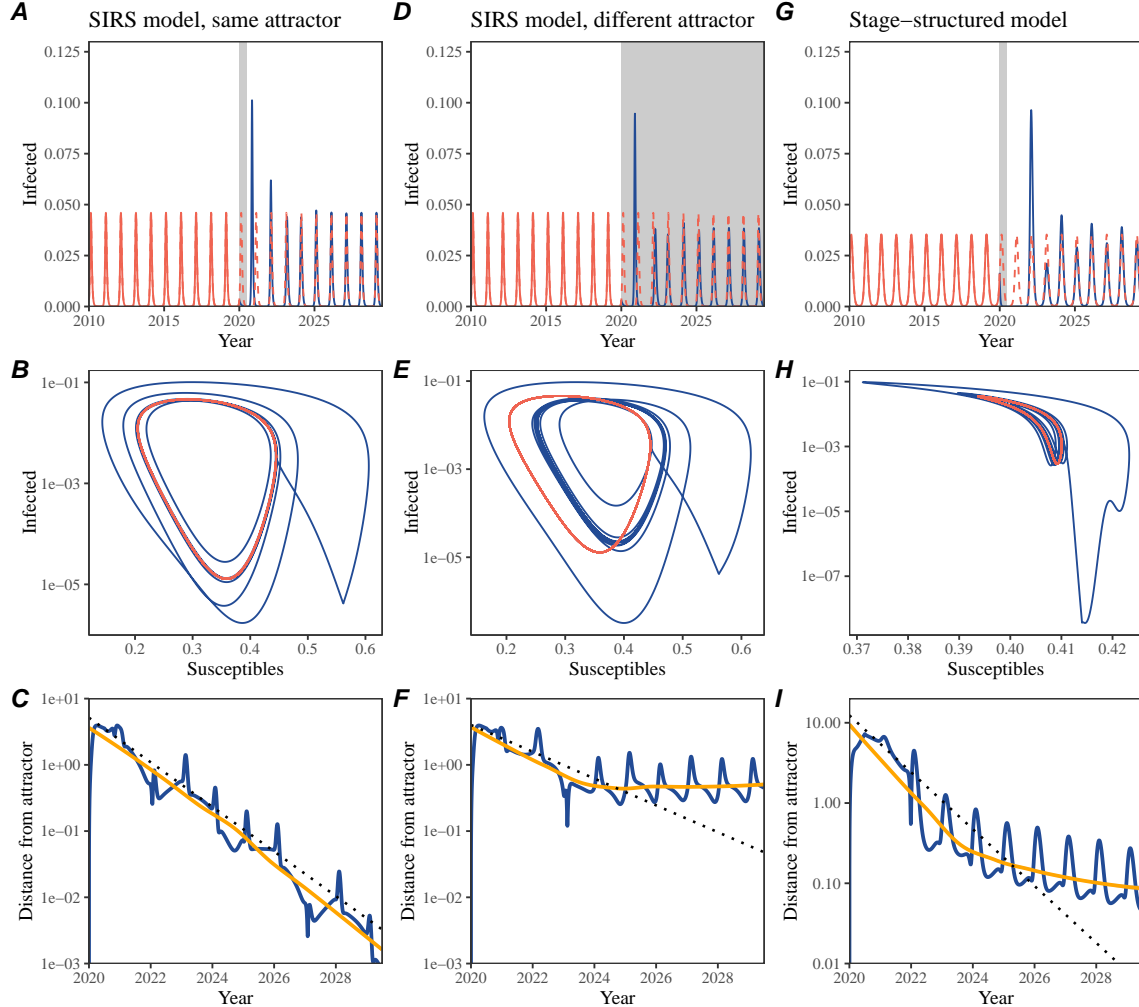


Figure 2: A simple method to measure pathogen resilience following NPIs across different scenarios. (A, D, G) Simulated epidemic trajectories across various models. Red and blue solid lines represent epidemic dynamics before and after interventions are introduced, respectively. Red dashed lines represent counterfactual epidemic dynamics in the absence of interventions. Gray regions indicate the duration of interventions. (B, E, H) Phase plane representation of the epidemic dynamics from corresponding models. Red and blue solid lines represent epidemic trajectories on an SI phase plane before and after interventions are introduced, respectively. (C, F, I) Changes in logged distance from the attractor over time. Blue lines represent the logged distance from the attractor. Orange lines represent the locally estimated scatterplot smoothing (LOESS) fits to the logged distance from attractor. Dotted lines show the intrinsic resilience of the seasonally unforced system.

117 structured system, but the rate of decrease decelerates with the damped oscillations
 118 (Figure 2I). This behavior is also referred to as a ghost attractor, which causes long

119 transient dynamics and slow transitions [16]. Strong seasonal forcing in transmission
120 can also lead to transient phenomena for a simple SIRS model, causing a slow return
121 to pre-perturbation dynamics (Supplementary Figure S1).

122 We also explore measuring the resilience of a two-strain host-pathogen system:
123 when the dynamics two strains (or two pathogens) are coupled through cross immu-
124 nity, we would expect the entire system to be characterized by a single resilience value
125 (rather than having two separate resilience for each strain). Simulations from a sim-
126 ple two-strain system illustrate that separate analyses of individual strain dynamics
127 (e.g., RSV A vs B) and a joint analysis of total infections (e.g., total RSV infections)
128 (Supplementary Figure S2, 3). *[SWP: This is expected because the phase portaits
129 of each of the coupled strains are projections of the shared attractor, according to
130 Takens Theorem. (Is this precisely correct?)]* Analogous to a single system, strong
131 seasonal forcing in transmission can cause the system to slow down through transient
132 phenomena (Supplementary Figure S4).

133 These observations indicate three possibilities. First, we can directly estimate
134 the empirical resilience of a host-pathogen system by looking at how fast the system
135 approaches a pre-pandemic attractor, provided that we can measure the distance
136 from attractor. The empirical approach to estimating pathogen resilience is partic-
137 ularly convenient because it does not require us to know the true underlying model;
138 estimating the intrinsic resilience from fitting misspecified models can lead to bi-
139 ased estimates (Supplementary Figure S5). Second, resilience estimates allow us to
140 make phenomenological predictions about the dynamics of a host-pathogen system
141 following a perturbation: assuming that the distance from the attractor will decrease
142 exponentially over time, we can obtain a ballpark estimate for when the system will
143 reach an attractor. Finally, deviation from an exponential decrease in the distance
144 from attractor can provide information about whether the system has reached an
145 alternative attractor, or a ghost attractor, that is different from the original, pre-
146 pandemic attractor. These alternative attractors may reflect continued perturbations
147 from permanent changes in transmission patterns as well as changes in immune land-
148 scapes.

149 Inferring pathogen resilience from real data

150 Based on these observations, we now lay out our approach to estimating pathogen
151 resilience from real data (Figure 3). We then test this approach against simulations
152 and apply it to real data.

153 So far, we focused on simple examples that assume a constant transmission re-
154 duction. However, in practice, the impact of NPIs on pathogen transmission is
155 likely more complex (Figure 3A), reflecting introduction and relaxation of various
156 intervention strategies. These complexities can lead to longer delays between the
157 introduction of NPIs and pathogen re-emergence as well as temporal variation in
158 outbreak sizes (Figure 3B): in this example, continued transmission reduction from

159 NPIs limits the size of the first outbreak in 2021 following the emergence, allowing
160 for a larger outbreak in 2022 when NPIs are further relaxed.

161 Previously, we relied on the dynamics of susceptible and infected hosts to com-
162 pute the distance from attractor (Figure 2), but information on susceptible hosts is
163 rarely available in practice. In addition, uncertainties in case counts due to observa-
164 tion error as well as the possibility of complex, multiannual attractor add challenges
165 to measuring the distance from attractor. To address these challenges, we first re-
166 construct an empirical attractor by utilizing Takens' theorem, which states that an
167 attractor of a nonlinear multidimensional system can be mapped onto a delayed em-
168 bedding [14]. Here, we use delayed copies of logged values of pre-pandemic cases
169 $C(t)$ (Figure 3C) to reconstruct the attractor:

$$\langle \log(C(t) + 1), \log(C(t - \tau) + 1), \dots, \log(C(t - (M - 1)\tau) + 1) \rangle, \quad (1)$$

170 where the delay τ and embedding dimension M are determined based on autocor-
171 relations and false nearest neighbors, respectively [17, 18]. We then apply the same
172 delay and embedding dimensions to the entire time series to determine the position
173 on a multi-dimensional state space (Figure 3D), which allows us to measure the
174 nearest neighbor distance between the current state of the system and the empirical
175 pre-pandemic attractor (Figure 3E). In principle, we can quantify how fast this dis-
176 tance decreases by fitting a linear regression on a log scale, where the slope of the
177 linear regression corresponds to pathogen resilience. Overall temporal variations in
178 the distance from attractor, especially the observed rate of decrease, appear robust
179 to choices about embedding delays and dimensions; using longer delays and higher
180 dimensions tends to smooth out temporal variations in the distance from attractor
181 (Supplementary Figure S6).

182 Complex changes in the distance from attractor suggest that estimating pathogen
183 resilience from linear regression will likely be sensitive to our choice of fitting win-
184 dows for the regression (Figure 3E). In Supplementary Materials, we explore an
185 automated window selection criterion for linear regression and test it against ran-
186 domized, stochastic simulations across a wide range of realistic NPI shapes. We find
187 that resilience estimates based on the automated window selection criteria are mod-
188 erately correlated ($\rho = 0.48$) with the intrinsic resilience of the post-NPI attractor
189 (Supplementary Figure S7). In contrast, a naive approach that uses the entire time
190 series, starting from the peak distance, only gives a correlation coefficient of $\rho = 0.09$
191 and consistently underestimates the intrinsic resilience (Supplementary Figure S7).

192 Now, we apply this approach to pathogen surveillance data presented in Figure
193 1. For each time series, we apply Takens' theorem independently to reconstruct the
194 empirical attractor and obtain the corresponding time series of distance from attrac-
195 tors (Supplementary Figure S8 for the distance time series and linear regression fits).
196 Then, we use the automated window selection criteria to fit a linear regression and
197 estimate the empirical resilience for each pathogen in each country. For most res-
198 piratory pathogens, resilience estimates fall between 0.4/year and 1.8/year (Figure
199 4A), with the exception of Rhinovirus in the US (0.066/year; 95% CI: 0.018/year–

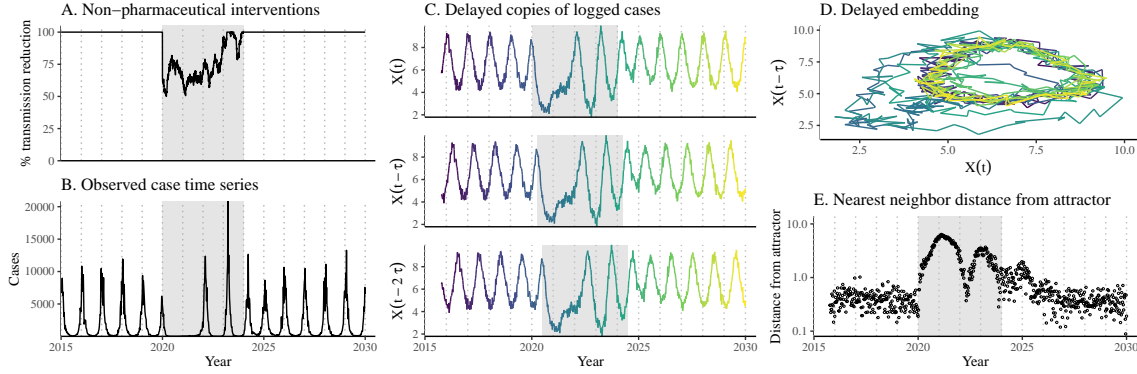


Figure 3: A schematic diagram explaining the inference of pathogen resilience from synthetic data. (A) A realistic example of a synthetic NPI, represented by a relative reduction in transmission. (B) The impact of the synthetic NPI on epidemic dynamics simulated using a SIRS model with demographic stochasticity. (C) Generating delayed copies of the logged time series allows us to obtain an embedding. (D) Two dimensional representation of an embedding. (E) Delayed embedding allows us to calculate the nearest neighbor distance from the empirical attractor, which is determined based on the pre-pandemic time series. This distance time series can be used to infer pathogen resilience after choosing an appropriate window for linear regression.

0.113/year) and Bocavirus in Korea (0.087/year; 95% CI: 0.023/year–0.151/year). Excluding these exceptions, the mean resilience of common respiratory pathogens is 0.974/year (95% CI: 0.784/year–1.16/year). As a reference, this is ≈ 7 times higher than the intrinsic resilience of pre-vaccination measles dynamics ($\approx 0.13/\text{year}$). Finally, resilience estimates for norovirus appears to be comparable to the intrinsic resilience of measles: 0.119/year (95%CI: 0.004/year–0.233/year) for Korea and 0.385/year (95% CI: 0.167/year–0.603/year). A simple ANOVA shows that there are significant differences in resilience estimates across countries ($p < 0.036$) and pathogens ($p < 0.030$).

Using resilience estimates, we now predict when each pathogen will return to their original pre-pandemic cycles. Specifically, we extend our linear regression fits to distance-from-attractor time series and ask when the predicted regression line will cross a threshold value, which we set to a mean of pre-pandemic distances. We predict that a return to pre-pandemic cycles would be imminent for most pathogens (Figure 4B; see Supplementary Figure S9 for a zoomed out version). In addition, we also predict that many pathogens should have already returned to their pre-pandemic dynamics by the end of 2024; but these predictions contradict some of the observed pathogen dynamics. For example, we predict that both human metapneumovirus and RSV in Korea should have returned to their attractors by now, but the magnitude and timing of recent epidemics are different from pre-pandemic patterns (Figure 1). These observations suggest the possibility that some common respiratory pathogens

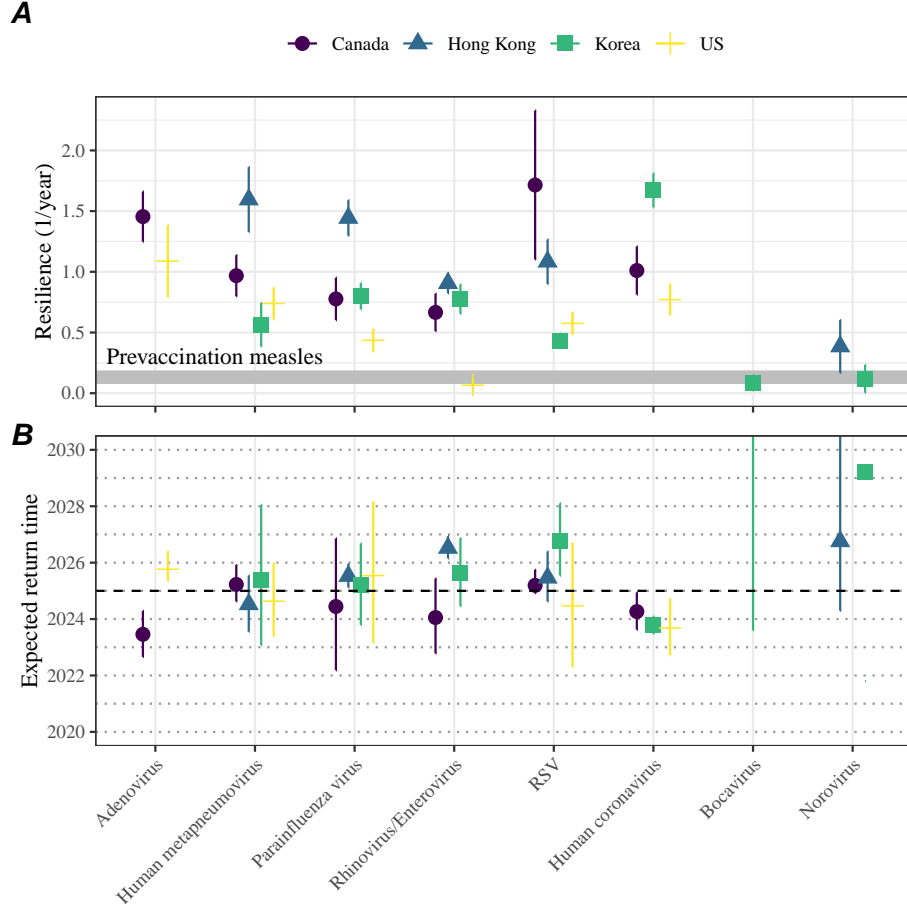


Figure 4: **Summary of resilience estimates.** (A) Estimated pathogen resilience. The gray horizontal line represents the intrinsic resilience of pre-vaccination measles dynamics. (B) Predicted timing of when each pathogen will return to their pre-pandemic cycles. The dashed line in panel B indicates the end of 2024 (current observation time). Error bars represent 95% confidence intervals.

221 may have converged to different attractors.

222 In Supplementary Materials, we also consider using a lower threshold for the false
 223 nearest neighbor approach when determining the embedding dimension; this gives
 224 a higher embedding dimension. As explained earlier (Supplementary Figure S6),
 225 this gives a smoother distance-from-attractor time series (compare Supplementary
 226 Figure S10 with S8); this also requires us to use longer time series, which prevents
 227 us from estimating resilience for some pathogens. Overall, resulting estimates of
 228 pathogen resilience with higher embedding dimensions still fall between 0.3/year
 229 and 2.1/year for the most part (Supplementary Figure S11). A direct comparison
 230 between two approaches (i.e., original estimate vs using higher dimensions) shows a
 231 strong consistency in resilience estimates (Supplementary Figure S12).

232 **Susceptible host dynamics explain variation in pathogen
233 resilience**

234 So far, we focused on quantifying pathogen resilience from the observed patterns of
235 pathogen re-emergence following COVID-19 interventions. But what factors deter-
236 mine how resilient a host-pathogen system is? Here, we use a standard Susceptible-
237 Infected-Recovered-Susceptible (SIRS) model to show that susceptible host dynamics
238 are the key determinants of pathogen resilience. To do so, we vary the basic reproduc-
239 tion number \mathcal{R}_0 , which represents the average number of secondary infections caused
240 by a newly infected individual in a fully susceptible population, and the duration of
241 immunity and compute intrinsic resilience for each parameter.

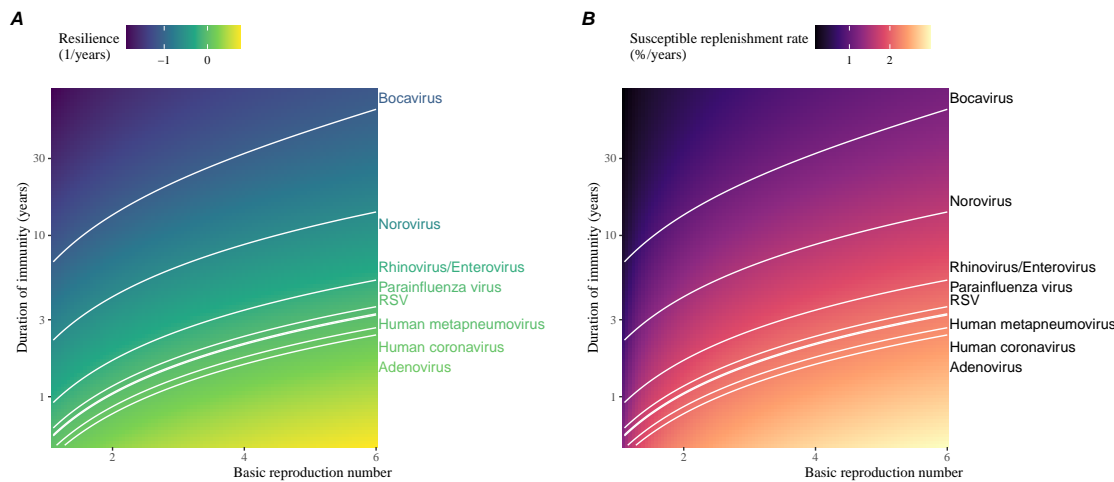


Figure 5: **Linking pathogen resilience to epidemiological parameters and susceptible host dynamics.** (A) The heat map represents intrinsic resilience as a function of the basic reproduction number \mathcal{R}_0 and the duration of immunity. (B) The heat map represents per-capita susceptible replenishment rate as a function of the basic reproduction number \mathcal{R}_0 and the duration of immunity. The standard SIRS model is used to compute intrinsic resilience and per-capita susceptible replenishment rate. Lines correspond to a set of parameters that are consistent with mean resilience estimates for each pathogen. Pathogens are ranked based on their mean resilience estimates, averaged across different countries.

242 We find an increase in \mathcal{R}_0 and a decrease in duration of immunity correspond
243 to an increase in pathogen resilience (Figure 5A). These variations can be under-
244 stood in terms of the susceptible host dynamics, where faster per-capita susceptible
245 replenishment rate causes the system to be more resilient (Figure 5B). This rate can
246 be expressed as a ratio between absolute rate at which new susceptibles enter the
247 population and the equilibrium number of susceptible individuals in the population,
248 \bar{S} . Therefore, both higher \mathcal{R}_0 and shorter duration of immunity can drive faster

249 per-capita susceptible replenishment rate (Figure 5B), especially because higher \mathcal{R}_0
250 leads to lower \bar{S} .

251 Finally, we can now rank different pathogens based on the average values of em-
252 pirical resilience, which allows us to determine a set of parameters that are consistent
253 with the estimated resilience (Figure 5A). Across all pathogens we consider, except
254 for bocavirus and norovirus, we estimate that the average duration of immunity is
255 likely to be short (< 6 years) across a plausible range of \mathcal{R}_0 . These rankings further
256 allow us to map each pathogen onto a set of parameters that are consistent with
257 its empirical resilience (Figure 5A) and obtain a plausible range of susceptible re-
258 plenishment rates for each pathogen (Figure 5B). However, we note that there is no
259 one-to-one correspondence between susceptible replenishment rates and pathogen re-
260 silience, leading to a wide uncertainty in the estimates for susceptible replenishment
261 rates (Figure 5B).

262 Discussion

263 The COVID-19 interventions have caused major disruptions to circulation patterns
264 of both respiratory and non-respiratory pathogens, adding challenges to predicting
265 their future dynamics [1, 2, 3, 4]. On the other hand, these interventions offer
266 large-scale natural experiments for understanding how different pathogens respond to
267 perturbations. In this study, we show that pathogen re-emergence patterns following
268 COVID-19 interventions can be characterized through the lens of ecological resilience.
269 Traditionally, ecological resilience measures how fast a system returns to a reference
270 state following a perturbation. In the context of respiratory pathogens, resilience
271 measures how fast epidemics return to their endemic cycles after interventions are
272 lifted.

273 We use an attractor reconstruction approach to quantify how distance from at-
274 tractor changes over time for each pathogen [14]. We show that the resilience of
275 a host-pathogen system can be estimated by fitting a linear regression to a logged
276 distance-from-attractor time series. Overall, we estimate that the resilience for most
277 common respiratory pathogens ranges between 0.4/year and 1.8/year, which is 3–14
278 times more resilient than prevaccination measles, indicating potential challenges in
279 controlling common respiratory pathogens.

280 Our framework allows us to make phenomenological predictions about when each
281 pathogen will return to their endemic cycles. The ability to predict future epidemic
282 patterns from resilience estimates offers a new paradigm for epidemic forecasting.
283 While this approach cannot predict the exact timing of outbreaks or epidemic pat-
284 terns, it is nonetheless useful for predicting when epidemics will settle down to regular
285 cycles after a large perturbation, such as COVID-19 interventions.

286 Our analyses suggest a possibility that several pathogens may have converged
287 to different endemic cycles compared to their pre-pandemic epidemic patterns. Key
288 examples include human metapnuemovirus, RSV, and bocavirus in Korea as well as

289 RSV in Hong Kong. These changes may reflect changes in surveillance or actual shift
290 in the dynamics, caused by permanent changes in behavior or population-level immu-
291 nity. While it seems unlikely that permanent changes in behavior would only affect a
292 few pathogens and not others, we cannot rule out this possibility given heterogeneity
293 in the age of infection across different respiratory pathogens [SWP: CITE]. A shift
294 in population-level immunity is plausible, as the emergence of SARS-CoV-2 and ex-
295 tinction of influenza B/Yamagata likely caused major changes in immune landscapes;
296 interactions among co-circulating pathogens, such as cross immunity between RSV
297 and HMPV [19], may have also contributed to changes in population-level immu-
298 nity. However, we currently do not know how immunity, or lack thereof, from these
299 pathogens would affect infection from other pathogens. Future studies should use
300 detailed mechanistic models, coupled with behavioral and immunological data, to
301 test these hypotheses and better understand post-pandemic dynamics of endemic
302 pathogens.

303 We show that susceptible host dynamics shape pathogen resilience, where faster
304 replenishment of the susceptible population causes the pathogen to be more resilient.
305 For simplicity, we focus on waning immunity and birth as a main driver of the suscep-
306 tible host dynamics but other mechanisms can also contribute to the replenishment
307 of the susceptible population. In particular, pathogen evolution, especially the emer-
308 gence of antigenically novel strains, can cause effective waning of immunity in the
309 population; therefore, we hypothesize that faster rates of antigenic evolution can also
310 cause a pathogen to be more resilient. Future studies should explore the relationship
311 between the rate of evolution and resilience for antigenically evolving pathogens.

312 Quantifying pathogen resilience also offers novel approaches to validating population-
313 level epidemiological models. So far, the majority of model validation in epidemiology
314 is based on the ability of a model to reproduce the observed epidemic dynamics and
315 to predict future dynamics [20, 19, 21, 22, 23]. However, there can be plethora of
316 models that meet these criteria. For example, two major RSV models have been pro-
317 posed so far to explain biennial epidemic patterns: (1) a stage- and age-structured
318 model that allows for disease severity to vary with number of past infections and
319 age of infection [21] and (2) a pathogen-interaction model that accounts for cross
320 immunity between RSV and human metapnuemovirus [19]. Since both models can
321 accurately reproduce the observed epidemic patterns, standard criteria for model
322 validation do not allow us to distinguish between these two models from population-
323 level data alone. Instead, we can measure the empirical resilience of each model
324 by simulating various perturbations and compare them to estimates of empirical re-
325 siliience from data, using COVID-19 interventions as an opportunity. Future studies
326 should further investigate using pathogen resilience for validating epidemic models.

327 There are several limitations to our work. First of all, we did not extensively ex-
328 plore other approaches to reconstructing the attractor. Recent studies showed that
329 more sophisticated approaches, such as using non-uniform embedding, can provide
330 more robust reconstruction for noisy data [18]. In the context of causal inference,
331 choices about embedding can have major impact on the resulting inference [24]. Our

resilience estimates are likely overly confident given a lack of uncertainties in attractor reconstruction as well as the simplicity of our statistical framework. Short pre-pandemic time series also contributes to the crudeness of our estimates. Nonetheless, as illustrated in our sensitivity analyses (Supplementary Figure S6, S10–S12), inferences about pathogen resilience appear to be robust to decisions about embedding lags and dimensions—this is because tracking the rate at which the system approaches the attractor is likely a much simpler problem than making inferences about causal directionality. Our qualitative prediction that common respiratory pathogens are more resilient than prevaccination measles is also likely to be robust to these predictions, given how rapid many respiratory pathogens returned to their original cycles following COVID-19 interventions.

Predicting the impact of anthropogenic changes on infectious disease dynamics is a fundamental aim of infectious disease research in a rapidly changing world. Our study illustrates that quantifying pathogen resilience can help us understand how infectious disease pathogens respond to major perturbations caused by public health interventions. More broadly, a detailed understanding of the determinants of pathogen resilience may offer unique insights into pathogen persistence and controllability.

Materials and Methods

Data

We gathered time series on respiratory infections from four different countries: Canada, Hong Kong, Korea, and United States (US). As a reference, we also included time series data on norovirus infections for available countries—in contrast to respiratory pathogens, we expect gastrointestinal viruses, such as norovirus, to be less affected by COVID-19 intervention measures. For all time series, we rounded every year to 52 weeks by taking the average number of cases and tests between the 52nd and 53rd week. We also rescale all time series to account for changes in testing patterns, which are then used for the actual analysis.

Weekly time series of respiratory infection cases in Canada comes from the Respiratory Virus Detection Surveillance System, which collect data from select laboratories across Canada. We extract the data from <https://www.canada.ca/en/public-health/services/surveillance/respiratory-virus-detections-canada.html>. To account for an increase in testing from 2013 to 2024, we calculate a 2 year moving average for the number of tests for each pathogen, which we use as a proxy for testing effort. Then, we divide the smoothed testing patterns by the smoothed value at the final week such that the testing effort has a maximum of 1. We then divide weekly cases by the testing effort to obtain a scaled case time series. A similar approach was used earlier for the analysis of RSV time series in the US [21].

Weekly time series of respiratory infection cases in Hong Kong comes from the Centre for Health Protection, Department of Health. We extract the data from

372 <https://www.chp.gov.hk/en/statistics/data/10/641/642/2274.html>. We also
373 apply the same scaling procedure to the time series as we did for Canada. For Hong
374 Kong, we only adjust for testing efforts up to the end of 2019 because there was a
375 major reduction in testing for common respiratory pathogens since 2020.

376 Weekly time series of acute respiratory infection cases in Korea comes from Ko-
377 rea Disease Control and Prevention Agency. We extract the data from <https://dportal.kdca.go.kr/pot/is/st/ari.do>. While we do not have information on
378 testing, the reported number of respiratory infections consistently increased from
379 2013 to the end of 2019, which we interpreted as changes in testing patterns. Since
380 we do not have testing numbers, we used the weekly sum of all acute respiratory vi-
381 ral infection cases as a proxy for testing, which were further smoothed with moving
382 averaged and scaled to have a maximum of 1. For Korea, we also only adjust for
383 testing efforts up to the end of 2019.

385 Finally, weekly time series of respiratory infection cases in the US comes from
386 the National Respiratory and Enteric Virus Surveillance System. In the US, there
387 has been a large increase in testing against some respiratory pathogens, especially
388 RSV, which could not be corrected for through simple scaling. Instead, we derive an
389 incidence proxy by multiplying the test positivity with influenza-like illness positivity,
390 which is taken from <https://gis.cdc.gov/grasp/fluvview/fluportaldashboard.html>.
391 This method of estimating an incidence proxy has been recently applied in
392 the analysis of seasonal coronaviruses [7] and Mycoplasma pneumoniae infections [4].
393 Detailed assumptions and justifications are provided in [25].

394 Estimating pathogen resilience

395 In order to measure pathogen resilience from surveillance data, we first reconstruct
396 the empirical pre-pandemic attractor of the system using Takens' embedding theorem
397 [14]. Specifically, for a given pathogen, we take the pre-pandemic (before 2020)
398 case time series $C(t)$ and reconstruct the attractor using delayed embedding with a
399 uniform delay of τ and dimension M :

$$X_{\tau,m}(t) = \langle \log(C(t) + 1), \log(C(t - \tau) + 1), \dots, \log(C(t - (M - 1)\tau) + 1) \rangle. \quad (2)$$

400 Here, the delay τ is determined by looking at the autocorrelation of the logged pre-
401 pandemic time series and asking when the autocorrelation crosses 0 for the first time
402 [18]; a typical delay for an annual outbreak is around 13 weeks.

403 Then, for a given delay τ , we determine the embedding dimension M using the
404 false nearest neighbors approach [17, 18]. To do so, we start with an embedding
405 dimension e and construct a set of points $A_{\tau,e} = \{X_{\tau,e}(t) | t < 2020\}$. Then, for
406 each point $X_{\tau,e}(t)$, we determine the nearest neighbor from the set $A_{\tau,e}$, which we
407 denote $X_{\tau,e}(t_{nn})$ for $t \neq t_{nn}$. Then, if the distance between these two points on $e + 1$
408 dimension, $D_{\tau,e+1}(t) = \|X_{\tau,e+1}(t_{nn}) - X_{\tau,e+1}(t)\|_2$, is larger than their distance on
409 e dimension, $D_{\tau,e}(t) = \|X_{\tau,e}(t_{nn}) - X_{\tau,e}(t)\|_2$, these two points are deemed to be
410 false nearest neighbors; specifically, we use a threshold R for the ratio between two

411 distances $D_{\tau,e+1}(t)/D_{\tau,e}(t)$ to determine false nearest neighbors. In the main text,
 412 we determine embedding dimension based as the first dimension without any false
 413 nearest neighbors for $R = 10$. In Supplementary Materials, we impose $R = 5$ to select
 414 for higher dimensions. Once we determine the embedding lag τ and dimension M ,
 415 we apply the embedding to the entire time series and calculate the nearest neighbor
 416 distance against the attractor $A_{\tau,M}$ to obtain a time series of distance from attractor
 417 $D_{\tau,M}(t)$.

418 From a time series of distance from attractor, we estimate pathogen resilience
 419 by fitting a linear regression to an appropriate window. To automatically select
 420 the fitting window, we begin by smoothing the distance time series using locally
 421 estimated scatterplot smoothing (LOESS) to obtain $\hat{D}_{\tau,M}(t)$, where the smoothing
 422 is performed on a log scale and exponentiated afterwards. Then, we determine
 423 threshold values (T_{start} and T_{end}) for the smoothed distances and choose the fitting
 424 window based on when $\hat{D}_{\tau,M}(t)$ crosses these threshold values for the first time.
 425 These thresholds are determined by first calculating maximum distance,

$$\max \hat{D} = \max \hat{D}_{\tau,M}(t), \quad (3)$$

426 and mean pre-pandemic distance,

$$\hat{D}_{\text{mean}} = \frac{1}{N_{t < 2020}} \sum_{t < 2020} \hat{D}_{\tau,M}(t), \quad (4)$$

427 as a reference, and then dividing their ratios into 10 equal bins:

$$T_{\text{start}} = \hat{D}_{\text{mean}} \times \left(\frac{\max \hat{D}}{\hat{D}_{\text{mean}}} \right)^{9/10} \quad (5)$$

$$T_{\text{end}} = \hat{D}_{\text{mean}} \times \left(\frac{\max \hat{D}}{\hat{D}_{\text{mean}}} \right)^{1/10} \quad (6)$$

428 This allows us to discard the initial period during which the distance increases (from
 429 the introduction of intervention measures) and the final period during which the
 430 distance plateaus (as the system reaches an attractor). The fitting window is deter-
 431 mined based on when the smoothed distance $\hat{D}_{\tau,M}(t)$ crosses these threshold values
 432 for the first time; then, we fit a linear regression to logged (unsmoothed) distances
 433 $\log D_{\tau,M}(t)$ using that window.

434 Mathematical modeling

435 Throughout the paper, we use a series of mathematical models to illustrate the con-
 436 cept of pathogen resilience and to understand the determinants of pathogen resilience.
 437 In general, the intrinsic resilience for a given system is given by the largest real part
 438 of the eigenvalues of the linearized system at endemic equilibrium. Here, we focus on

439 the SIRS model and present the details of other models in Supplementary Materials.
 440 The SIRS (Susceptible-Infected-Recovered-Susceptible) model is the simplest model
 441 that allows for waning of immunity, where recovered (immune) individuals are as-
 442 sumed to become fully susceptible after an average of $1/\delta$ time period. The dynamics
 443 of the SIRS model is described by the following set of differential equations:

$$\frac{dS}{dt} = \mu - \beta(t)SI - \mu S + \delta R \quad (7)$$

$$\frac{dI}{dt} = \beta(t)SI - (\gamma + \mu)I \quad (8)$$

$$\frac{dR}{dt} = \gamma I - (\delta + \mu)R \quad (9)$$

(10)

444 where μ represents the birth/death rate, $\beta(t)$ represents the time-varying trans-
 445 mission rate, and γ represents the recovery rate. The basic reproduction number
 446 $\mathcal{R}_0 = \beta(t)/(\gamma + \mu)$ is defined as the average number of secondary infections caused
 447 by a single infected individual in a fully susceptible population and measures the
 448 intrinsic transmissibility of a pathogen.

449 When we first introduce the idea of pathogen resilience (Figure 2), we impose
 450 sinusoidal changes to the transmission rate to account for seasonal transmission:

$$\beta(t) = b_1(1 + \theta \cos(2\pi(t - \phi)))\alpha(t), \quad (11)$$

451 where b_1 represents the baseline transmission rate, θ represents the seasonal ampli-
 452 tude, and ϕ represents the seasonal offset term. Here, we also introduce an extra
 453 multiplicative term $\alpha(t)$ to account for the impact of COVID-19 interventions, where
 454 $\alpha(t) < 1$ indicates transmission reduction. Figure 2A and 2B are generated assuming
 455 $b_1 = 3 \times (365/7 + 1/50)/\text{years}$, $\theta = 0.2$, $\phi = 0$, $\mu = 1/50/\text{years}$, $\gamma = 365/7/\text{years}$, and
 456 $\delta = 1/2/\text{years}$. In Figure 2A, we impose a 50% transmission reduction for 6 months
 457 from 2020:

$$\alpha(t) = \begin{cases} 0.5 & 2020 \leq t < 2020.5 \\ 1 & \text{otherwise} \end{cases} \quad (12)$$

458 In Figure 2B, we impose a 50% transmission reduction for 6 months from 2020 and
 459 a permanent 10% reduction onward:

$$\alpha(t) = \begin{cases} 1 & t < 2020 \\ 0.5 & 2020 \leq t < 2020.5 \\ 0.9 & 2020.5 \leq t \end{cases} \quad (13)$$

460 In both scenarios, we simulate the SIRS model from the following initial conditions
 461 ($S(0) = 1/\mathcal{R}_0$, $I(0) = 1 \times 10^{-6}$, and $R(0) = 1 - S(0) - I(0)$) from 1900 until 2030.

462 To measure the empirical resilience of the SIR model (Figure 2C and 2F), we
 463 compute the normalized distance between post-intervention susceptible and logged

⁴⁶⁴ infected proportions and their corresponding pre-intervention values at the same time
⁴⁶⁵ of year:

$$\sqrt{\left(\frac{S(t) - S_{\text{pre}}(t)}{\sigma_S}\right)^2 + \left(\frac{\log I(t) - \log I_{\text{pre}}(t)}{\sigma_{\log I}}\right)^2}, \quad (14)$$

⁴⁶⁶ where σ_S and $\sigma_{\log I}$ represent the standard deviation in the pre-intervention suscep-
⁴⁶⁷ tible and logged infected proportions. We normalize the differences in susceptible
⁴⁶⁸ and logged infected proportions to allow both quantities to equally contribute to the
⁴⁶⁹ changes in distance from attractor. In Supplementary Materials, we also compare
⁴⁷⁰ the how the degree of seasonal transmission affects empirical resilience by varying
⁴⁷¹ θ from 0 to 0.4; when we assume no seasonality ($\theta = 0$), we do not normalize the
⁴⁷² distance because the standard deviation of pre-intervention dynamics are zero.

⁴⁷³ Finally, we use the SIRS model to understand how underlying epidemiological
⁴⁷⁴ parameters affect pathogen resilience and link this relationship to underlying sus-
⁴⁷⁵ ceptible host dynamics. For the simple SIRS model without seasonal transmission
⁴⁷⁶ ($\theta = 0$), the intrinsic resilience corresponds to:

$$-\frac{\text{Re}(\lambda)}{2} = \frac{\delta + \beta I^* + \mu}{2}. \quad (15)$$

⁴⁷⁷ Here, I^* represents the prevalence values at endemic equilibrium:

$$I^* = \frac{(\delta + \mu)(\beta - (\gamma + \mu))}{\beta(\delta + \gamma + \mu)}. \quad (16)$$

⁴⁷⁸ The susceptible replenishment rate is given by:

$$S_{\text{replenish}} = \frac{\mu + \delta R}{S^*}, \quad (17)$$

⁴⁷⁹ where $S^* = 1/\mathcal{R}_0$ represents the equilibrium proportion of susceptible individuals.
⁴⁸⁰ We vary the basic reproduction number \mathcal{R}_0 between 1.1 to 6 and the average duration
⁴⁸¹ of immunity $1/\delta$ between 2 to 80 years, and compute these two quantities. In doing
⁴⁸² so, we fix all other parameters: $\mu = 1/80/\text{years}$ and $\gamma = 365/7/\text{years}$.

483 **Supplementary Text**

484 **Resilience of a stage-structured system.**

485 In Figure 2G–I, we use a more realistic, stage-structured model to illustrate how
 486 transient phenomena can cause the system to slow down. Specifically, we use the
 487 stage-structured RSV model proposed by [21], which assumes that subsequent rein-
 488 fections cause an individual to become less susceptible and transmissible than previ-
 489 ous infections. The model dynamics can be described as follows:

$$\frac{dM}{dt} = \mu - (\omega + \mu)M \quad (S1)$$

$$\frac{dS_0}{dt} = \omega M - (\lambda(t) + \mu)S_0 \quad (S2)$$

$$\frac{dI_1}{dt} = \lambda(t)S_0 - (\gamma_1 + \mu)I_1 \quad (S3)$$

$$\frac{dS_1}{dt} = \gamma_1 I_1 - (\sigma_1 \lambda(t) + \mu)S_1 \quad (S4)$$

$$\frac{dI_2}{dt} = \sigma_1 \lambda(t)S_1 - (\gamma_2 + \mu)I_2 \quad (S5)$$

$$\frac{dS_2}{dt} = \gamma_2 I_2 - (\sigma_2 \lambda(t) + \mu)S_2 \quad (S6)$$

$$\frac{dI_3}{dt} = \sigma_2 \lambda(t)S_2 - (\gamma_3 + \mu)I_3 \quad (S7)$$

$$\frac{dS_3}{dt} = \gamma_3 I_3 - (\sigma_3 \lambda(t) + \mu)S_3 + \gamma_4 I_4 \quad (S8)$$

$$\frac{dI_4}{dt} = \sigma_3 \lambda(t)S_3 - (\gamma_4 + \mu)I_4 \quad (S9)$$

(S10)

490 where M represents the proportion of individuals who are maternally immune; S_i
 491 represents the proportion of individuals who are susceptible after i prior infections; I_i
 492 represents the proportion of individuals who are currently (re)-infected with their i -th
 493 infection; μ represents the birth and death rates; $1/\omega$ represents the mean duration
 494 of maternal immunity; $1/\gamma_i$ represents the mean duration of infection; $\lambda(t)$ represents
 495 the force of infection; and σ_i represents the reduction in susceptibility for reinfection.
 496 The force of infection is modeled using a sinusoidal function:

$$\beta(t) = b_1(1 + \theta \cos(2\pi(t - \phi)))\alpha(t) \quad (S11)$$

$$\lambda(t) = \beta(I_1 + \rho_1 I_2 + \rho_2(I_3 + I_4)), \quad (S12)$$

497 where b_1 represents the baseline transmission rate; θ represents the seasonal ampli-
 498 tude; ϕ represents the seasonal offset term; $\alpha(t)$ represents the intervention effect;
 499 and ρ_i represents the impact of immunity on transmission reduction. We use the

500 following parameters to simulate the impact of interventions on epidemic dynam-
 501 ics [21]: $b_1 = 9 \times (365/10 + 1/80)/\text{years}$, $\theta = 0.2$, $\phi = -0.1$, $\omega = 365/112/\text{years}$,
 502 $\gamma_1 = 365/10/\text{years}$, $\gamma_2 = 365/7/\text{years}$, $\gamma_3 = 365/5/\text{years}$, $\sigma_1 = 0.76$, $\sigma_2 = 0.6$,
 503 $\sigma_3 = 0.4$, $\rho_1 = 0.75$, $\rho_2 = 0.51$, and $\mu = 1/80/\text{years}$. We assume a 50% transmission
 504 reduction for 6 months from 2020:

$$\alpha(t) = \begin{cases} 0.5 & 2020 \leq t < 2020.5 \\ 1 & \text{otherwise} \end{cases} \quad (\text{S13})$$

505 The model is simulated from 1900 to 2030 using the following initial conditions:
 506 $M = 0$, $S_0 = 1/\mathcal{R}_0 - I_1$, $I_1 = 1 \times 10^{-6}$, $S_1 = 1 - 1/\mathcal{R}_0$, $I_2 = 0$, $S_2 = 0$, $I_3 = 0$,
 507 $S_3 = 0$, and $I_4 = 0$. For the phase plane analysis (Figure 2H) and distance analysis
 508 (Figure 2I), we rely on the average susceptibility,

$$\bar{S} = S_0 + \sigma_1 S_1 + \sigma_2 S_2 + \sigma_3 S_3, \quad (\text{S14})$$

509 and total prevalence,

$$I_{\text{total}} = I_1 + I_2 + I_3 + I_4. \quad (\text{S15})$$

510 These quantities are used to compute the normalized distance from the attractor, as
 511 described in the main text.

512 Resilience of a multistrain system.

513 We use a simple two-strain model to show that a multistrain host-pathogen system
 514 that is coupled through cross immunity can be described by a single resilience value.
 515 The model dynamics can be described as follows [19]:

$$\frac{dS}{dt} = \mu - \mu S - (\lambda_1 + \lambda_2)S + \rho_1 R_1 + \rho_2 R_2 \quad (\text{S16})$$

$$\frac{dI_1}{dt} = \lambda_1 S - (\gamma_1 + \mu)I_1 \quad (\text{S17})$$

$$\frac{dI_2}{dt} = \lambda_2 S - (\gamma_2 + \mu)I_2 \quad (\text{S18})$$

$$\frac{dR_1}{dt} = \gamma_1 I_1 - \lambda_2 \epsilon_{21} R_1 - \rho_1 R_1 + \rho_2 R - \mu R_1 \quad (\text{S19})$$

$$\frac{dR_2}{dt} = \gamma_2 I_2 - \lambda_1 \epsilon_{12} R_2 - \rho_2 R_2 + \rho_1 R - \mu R_2 \quad (\text{S20})$$

$$\frac{dJ_1}{dt} = \lambda_1 \epsilon_{12} R_2 - (\gamma_1 + \mu) J_1 \quad (\text{S21})$$

$$\frac{dJ_2}{dt} = \lambda_2 \epsilon_{21} R_1 - (\gamma_2 + \mu) J_2 \quad (\text{S22})$$

$$\frac{dR}{dt} = \gamma_1 J_1 + \gamma_2 J_2 - \rho_1 R - \rho_2 R - \mu R \quad (\text{S23})$$

516 where S represents the proportion of individuals who are fully susceptible to infections
 517 by both strains; I_1 represents the proportion of individuals who are infected with strain 1 without prior immunity; I_2 represents the proportion of individuals who are infected with strain 2 without prior immunity; R_1 represents the proportion of individuals who are fully immune against strain 1 and partially susceptible to reinfection by strain 2; R_2 represents the proportion of individuals who are fully immune against strain 2 and partially susceptible to reinfection by strain 1; J_1 represents the proportion of individuals who are infected with strain 1 with prior immunity against strain 2; J_2 represents the proportion of individuals who are infected with strain 2 with prior immunity against strain 1; R represents the proportion of individuals who are immune to infections from both strains; μ represents the birth/death rate; λ_1 and λ_2 represent the force of infection from strains 1 and 2, respectively; ρ_1 and ρ_2 represent the waning immunity rate; γ_1 and γ_2 represent the recovery rate; ϵ_{12} and ϵ_{21} represent the susceptibility to reinfection with strains 2 and 1, respectively, given prior immunity from infection with strains 1 and 2, respectively. The force of infection is modeled as follows:

$$\beta_1 = b_1(1 + \theta_1 \sin(2\pi(t - \phi_1)))\alpha(t) \quad (\text{S24})$$

$$\beta_2 = b_2(1 + \theta_2 \sin(2\pi(t - \phi_2)))\alpha(t) \quad (\text{S25})$$

$$\lambda_1 = \beta_1(I_1 + J_1) \quad (\text{S26})$$

$$\lambda_2 = \beta_2(I_2 + J_2) \quad (\text{S27})$$

532 In Supplementary Figures S2–S4, we assume the following parameters: $b_1 = 2 \times$
 533 $52/\text{years}$, $b_2 = 4 \times 52/\text{years}$, $\phi_1 = \phi_2 = 0$, $\epsilon_{12} = 0.9$, $\epsilon_{21} = 0.5$, $\gamma_1 = \gamma_2 = 52/\text{years}$,
 534 $\rho_1 = \rho_2 = 1/\text{years}$, and $\mu = 1/70/\text{years}$. For all simulations, we assume a 50%
 535 transmission reduction for 6 months from 2020:

$$\alpha(t) = \begin{cases} 0.5 & 2020 \leq t < 2020.5 \\ 1 & \text{otherwise} \end{cases} \quad (\text{S28})$$

536 The seasonal amplitude θ is varied from 0 to 0.4. All simulations are ran from 1900
 537 to 2030 from the following initial conditions: $S(0) = 1 - 2 \times 10^{-6}$, $I_1(0) = 1 \times 10^{-6}$,
 538 $I_2(0) = 1 \times 10^{-6}$, $R_1(0) = 0$, $R_2(0) = 0$, $J_1(0) = 0$, $J_2(0) = 0$, and $R(0) = 0$.

539 For this, we consider three different scenarios for measuring pathogen resilience:
 540 (1) we only have information about strain 1, (2) we only have information about
 541 strain 2, and (3) we are unable to distinguish the differences between strains. In
 542 the first two scenarios (see panels A–C for strain 1 and panels D–F for strain 2), we
 543 consider the dynamics of average susceptibility for each strain and total prevalence:

$$\bar{S}_1 = S + \epsilon_{12}R_2 \quad (\text{S29})$$

$$\hat{I}_1 = I_1 + J_1 \quad (\text{S30})$$

$$\bar{S}_2 = S + \epsilon_{21}R_1 \quad (\text{S31})$$

$$\hat{I}_2 = I_2 + J_2 \quad (\text{S32})$$

⁵⁴⁴ In the third scenario (panels G–I), we consider the dynamics of total susceptible and
⁵⁴⁵ infected population:

$$\hat{S} = S + R_2 + R_1 \quad (\text{S33})$$

$$\hat{I} = I_1 + J_1 + I_2 + J_2 \quad (\text{S34})$$

$$(\text{S35})$$

⁵⁴⁶ These quantities are used to compute the normalized distance from the attractor, as
⁵⁴⁷ described in the main text.

⁵⁴⁸ Estimating intrinsic resilience using mechanistic model

⁵⁴⁹ We test whether we can reliably estimate the intrinsic resilience of a system by fitting
⁵⁵⁰ a mechanistic model. Specifically, we simulate case time series from stochastic SIRS
⁵⁵¹ and two-strain models and fit a simple, deterministic SIRS model using a Bayesian
⁵⁵² framework.

⁵⁵³ First, we describe the simulation set up. The stochastic SIRS model can be
⁵⁵⁴ written as follows:

$$\beta(t) = \mathcal{R}_0 \left(1 + \theta \cos \left(\frac{2\pi t}{364} \right) \right) \alpha(t)(1 - \exp(-\gamma)) \quad (\text{S36})$$

$$\text{FOI}(t) = \beta(t)I(t - \Delta t)/N \quad (\text{S37})$$

$$B(t) \sim \text{Poisson}(\mu N) \quad (\text{S38})$$

$$\Delta S(t) \sim \text{Binom}(S(t - \Delta t), 1 - \exp(-(\text{FOI}(t) + \mu)\Delta t)) \quad (\text{S39})$$

$$N_{SI}(t) \sim \text{Binom}\left(\Delta S(t), \frac{\text{FOI}(t)}{\text{FOI}(t) + \mu}\right) \quad (\text{S40})$$

$$\Delta I(t) \sim \text{Binom}(I(t - \Delta t), 1 - \exp(-(\gamma + \mu)\Delta t)) \quad (\text{S41})$$

$$N_{IR}(t) \sim \text{Binom}\left(\Delta I(t), \frac{\gamma}{\gamma + \mu}\right) \quad (\text{S42})$$

$$\Delta R(t) \sim \text{Binom}(R(t - \Delta t), 1 - \exp(-(\delta + \mu)\Delta t)) \quad (\text{S43})$$

$$N_{RS}(t) \sim \text{Binom}\left(\Delta R(t), \frac{\delta}{\delta + \mu}\right) \quad (\text{S44})$$

$$S(t) = S(t - \Delta t) + N_{RS}(t) + B(t) - \Delta S(t) \quad (\text{S45})$$

$$I(t) = I(t - \Delta t) + N_{SI}(t) - \Delta I(t) \quad (\text{S46})$$

$$R(t) = R(t - \Delta t) + N_{IR}(t) - \Delta R(t) \quad (\text{S47})$$

⁵⁵⁵ where FOI represent the force of infection; N_{ij} represent the number of individuals
⁵⁵⁶ moving from compartment i to j on a given day; and $B(t)$ represents the number
⁵⁵⁷ of new births. We simulate the model on a daily scale—assuming 364 days in a
⁵⁵⁸ year so that it can be evenly grouped into 52 weeks—with the following parameters:
⁵⁵⁹ $\mathcal{R}_0 = 3$, $\theta = 0.1$, $\gamma = 1/7/\text{days}$, $\delta = 1/(364 \times 2)/\text{days}$, $\mu = 1/(364 \times 50)/\text{days}$, and

560 $N = 1 \times 10^8$. The model is simulated from 1900 to 2030 assuming $S(0) = N/3$,
561 $I(0) = 100$, and $R(0) = N - S(0) - I(0)$. The observed incidence from the model is
562 then simulated as follows:

$$C(t) = \text{Beta} - \text{Binom}(N_{SI}(t), \rho, k), \quad (\text{S48})$$

563 where ρ represents the reporting probability and k represents the overdispersion pa-
564 rameter of beta-binomial distribution. We assume $\rho = 0.002$ (i.e., 0.2% probability)
565 and $k = 1000$.

566 The stochastic two-strain model can be written as follows:

$$\beta_1(t) = b_1 \left(1 + \theta_1 \cos \left(\frac{2\pi(t - \phi_1)}{364} \right) \right) \alpha(t) \quad (\text{S49})$$

$$\beta_2(t) = b_2 \left(1 + \theta_2 \cos \left(\frac{2\pi(t - \phi_2)}{364} \right) \right) \alpha(t) \quad (\text{S50})$$

$$\text{FOI}_1(t) = \beta_1(t)(I_1(t - \Delta t) + J_1(t - \Delta t))/N \quad (\text{S51})$$

$$\text{FOI}_2(t) = \beta_2(t)(I_2(t - \Delta t) + J_2(t - \Delta t))/N \quad (\text{S52})$$

$$B(t) \sim \text{Poisson}(\mu N) \quad (\text{S53})$$

$$\Delta S(t) \sim \text{Binom}(S(t - \Delta t), 1 - \exp(-(\text{FOI}_1(t) + \text{FOI}_2(t) + \mu)\Delta t)) \quad (\text{S54})$$

$$N_{SI_1}(t) \sim \text{Binom}\left(\Delta S(t), \frac{\text{FOI}_1(t)}{\text{FOI}_1(t) + \text{FOI}_2(t) + \mu}\right) \quad (\text{S55})$$

$$N_{SI_2}(t) \sim \text{Binom}\left(\Delta S(t), \frac{\text{FOI}_2(t)}{\text{FOI}_1(t) + \text{FOI}_2(t) + \mu}\right) \quad (\text{S56})$$

$$\Delta I_1(t) \sim \text{Binom}(I_1(t - \Delta t), 1 - \exp(-(\gamma_1 + \mu)\Delta t)) \quad (\text{S57})$$

$$N_{I_1 R_1}(t) \sim \text{Binom}\left(\Delta I_1(t), \frac{\gamma_1}{\gamma_1 + \mu}\right) \quad (\text{S58})$$

$$\Delta I_2(t) \sim \text{Binom}(I_2(t - \Delta t), 1 - \exp(-(\gamma_2 + \mu)\Delta t)) \quad (\text{S59})$$

$$N_{I_2 R_2}(t) \sim \text{Binom}\left(\Delta I_2(t), \frac{\gamma_2}{\gamma_2 + \mu}\right) \quad (\text{S60})$$

$$\Delta R_1(t) \sim \text{Binom}(R_1(t - \Delta t), 1 - \exp(-(\epsilon_{21}\text{FOI}_2(t) + \rho_1 + \mu)\Delta t)) \quad (\text{S61})$$

$$N_{R_1 S}(t) \sim \text{Binom}\left(\Delta R_1(t), \frac{\rho_1}{\epsilon_{21}\text{FOI}_2(t) + \rho_1 + \mu}\right) \quad (\text{S62})$$

$$N_{R_1 J_2}(t) \sim \text{Binom}\left(\Delta R_1(t), \frac{\epsilon_{21}\text{FOI}_2(t)}{\epsilon_{21}\text{FOI}_2(t) + \rho_1 + \mu}\right) \quad (\text{S63})$$

$$\Delta R_2(t) \sim \text{Binom}(R_2(t - \Delta t), 1 - \exp(-(\epsilon_{12}\text{FOI}_1(t) + \rho_2 + \mu)\Delta t)) \quad (\text{S64})$$

$$N_{R_2 S}(t) \sim \text{Binom}\left(\Delta R_2(t), \frac{\rho_2}{\epsilon_{12}\text{FOI}_1(t) + \rho_2 + \mu}\right) \quad (\text{S65})$$

$$N_{R_2 J_1}(t) \sim \text{Binom}\left(\Delta R_2(t), \frac{\epsilon_{12}\text{FOI}_1(t)}{\epsilon_{12}\text{FOI}_1(t) + \rho_2 + \mu}\right) \quad (\text{S66})$$

$$\Delta J_1(t) \sim \text{Binom}(J_1(t - \Delta t), 1 - \exp(-(\gamma_1 + \mu)\Delta t)) \quad (\text{S67})$$

$$N_{J_1R}(t) \sim \text{Binom}\left(\Delta J_1(t), \frac{\gamma_1}{\gamma_1 + \mu}\right) \quad (\text{S68})$$

$$\Delta J_2(t) \sim \text{Binom}(J_2(t - \Delta t), 1 - \exp(-(\gamma_2 + \mu)\Delta t)) \quad (\text{S69})$$

$$N_{J_2R}(t) \sim \text{Binom}\left(\Delta J_2(t), \frac{\gamma_2}{\gamma_2 + \mu}\right) \quad (\text{S70})$$

$$\Delta R(t) \sim \text{Binom}(R(t - \Delta t), 1 - \exp(-(\rho_1 + \rho_2 + \mu)\Delta t)) \quad (\text{S71})$$

$$N_{RR_1}(t) \sim \text{Binom}\left(\Delta R(t), \frac{\rho_1}{\rho_1 + \rho_2 + \mu}\right) \quad (\text{S72})$$

$$N_{RR_2}(t) \sim \text{Binom}\left(\Delta R(t), \frac{\rho_2}{\rho_1 + \rho_2 + \mu}\right) \quad (\text{S73})$$

$$S(t) = S(t - \Delta t) - \Delta S(t) + B(t) + N_{R_1S}(t) + N_{R_2S}(t) \quad (\text{S74})$$

$$I_1(t) = I_1(t - \Delta t) - \Delta I_1(t) + N_{SI_1}(t) \quad (\text{S75})$$

$$I_2(t) = I_2(t - \Delta t) - \Delta I_2(t) + N_{SI_2}(t) \quad (\text{S76})$$

$$R_1(t) = R_1(t - \Delta t) - \Delta R_1(t) + N_{I_1R_1}(t) + N_{RR_1}(t) \quad (\text{S77})$$

$$R_2(t) = R_2(t - \Delta t) - \Delta R_2(t) + N_{I_2R_2}(t) + N_{RR_2}(t) \quad (\text{S78})$$

$$J_1(t) = J_1(t - \Delta t) - \Delta J_1(t) + N_{R_2J_1}(t) \quad (\text{S79})$$

$$J_2(t) = J_2(t - \Delta t) - \Delta J_2(t) + N_{R_1J_2}(t) \quad (\text{S80})$$

$$R(t) = R(t - \Delta t) - \Delta R(t) + N_{J_1R}(t) + N_{J_2R}(t) \quad (\text{S81})$$

567 We simulate the model on a daily scale with previously estimated parameters for the
 568 RSV-HMPV interaction [19]: $b_1 = 1.7/\text{weeks}$, $b_2 = 1.95/\text{weeks}$, $\theta_1 = 0.4$, $\theta_2 = 0.3$,
 569 $\phi_1 = 0.005 \times 7/364$, $\phi_2 = 4.99 \times 7/364$, $\epsilon_{12} = 0.92$, $\epsilon_{21} = 0.45$, $\gamma_1 = 1/10/\text{days}$,
 570 $\gamma_2 = 1/10/\text{days}$, $\rho_1 = 1/364/\text{days}$, $\rho_2 = 1/364/\text{days}$, $\mu = 1/(70 \times 364)/\text{days}$, and
 571 $N = 1 \times 10^8$. The model is simulated from 1900 to 2030 assuming $S(0) = N - 200$,
 572 $I_1(0) = 100$, $I_2(0) = 100$, $R_1(0) = 0$, $R_2(0) = 0$, $J_1(0) = 0$, $J_2(0) = 0$, and $R(0) = 0$.
 573 The observed incidence for each strain is then simulated as follows:

$$C_1(t) = \text{Beta} - \text{Binom}(N_{SI_1}(t) + N_{R_2J_1}, \rho, k), \quad (\text{S82})$$

$$C_2(t) = \text{Beta} - \text{Binom}(N_{SI_2}(t) + N_{R_1J_2}, \rho, k), \quad (\text{S83})$$

574 where ρ represents the reporting probability and k represents the overdispersion pa-
 575 rameter of beta-binomial distribution. We assume $\rho = 0.002$ (i.e., 0.2% probability)
 576 and $k = 500$. We also consider the total incidence: $C_{\text{total}}(t) = C_1(t) + C_2(t)$.

577 For both models, we consider a more realistic challenges in intervention effects
 578 $\alpha(t)$ to challenge our ability to estimate the intervention effects. Thus, we assume
 579 a 40% transmission reduction for 3 months from March 2020, followed by a 10%
 580 transmission reduction for 6 months, 20% transmission reduction for 3 months, and

581 a final return to normal levels:

$$\alpha(t) = \begin{cases} 1 & t < 2020.25 \\ 0.6 & 2020.25 \leq t < 2020.5 \\ 0.9 & 2020.5 \leq t < 2021 \\ 0.8 & 2021 \leq t < 2021.25 \\ 1 & 2021.25 \leq t \end{cases}. \quad (\text{S84})$$

582 For all simulations, we truncate the time series from the beginning of 2014 to the
583 end of 2023 and aggregate them into weekly cases.

584 To infer intrinsic resilience from time series, we fit a simple discrete time, deter-
585 ministic SIRS model [4]:

$$\Delta t = 1 \text{ week} \quad (\text{S85})$$

$$\text{FOI}(t) = \beta(t)(I(t - \Delta t) + \omega)/N \quad (\text{S86})$$

$$\Delta S(t) = [1 - \exp(-(\text{FOI}(t) + \mu)\Delta t)] S(t - \Delta t) \quad (\text{S87})$$

$$N_{SI}(t) = \frac{\text{FOI}(t)\Delta S(t)}{\text{FOI}(t) + \mu} \quad (\text{S88})$$

$$\Delta I(t) = [1 - \exp(-(\gamma + \mu)\Delta t)] I(t - \Delta t) \quad (\text{S89})$$

$$N_{IR}(t) = \frac{\gamma \Delta I(t)}{\gamma + \mu} \quad (\text{S90})$$

$$\Delta R(t) = [1 - \exp(-(\nu + \mu)\Delta t)] R(t - \Delta t) \quad (\text{S91})$$

$$N_{RS}(t) = \frac{\nu \Delta R(t)}{\nu + \mu} \quad (\text{S92})$$

$$S(t) = S(t - \Delta t) + \mu S - \Delta S(t) + N_{RS}(t) \quad (\text{S93})$$

$$I(t) = I(t - \Delta t) - \Delta I(t) + N_{SI}(t) \quad (\text{S94})$$

$$R(t) = R(t - \Delta t) - \Delta R(t) + N_{IR}(t) \quad (\text{S95})$$

586 where we include an extra term ω to account for external infections. Although actual
587 simulations do not include any external infections, we found that including this term
588 generally helped with model convergence in previous analyses [4]. The transmission
589 rate is divided into a seasonal term $\beta_{\text{seas}}(t)$ (repeated every year) and intervention
590 term $\alpha(t)$, which are estimated jointly:

$$\beta(t) = \beta_{\text{seas}}(t)\alpha(t), \quad (\text{S96})$$

591 where $\alpha < 1$ corresponds to reduction in transmission due to intervention effects. To
592 constrain the smoothness of $\beta_{\text{seas}}(t)$, we impose cyclic, random-walk priors:

$$\beta_{\text{seas}}(t) \sim \text{Normal}(\beta_{\text{seas}}(t - 1), \sigma) \quad t = 2 \dots 52 \quad (\text{S97})$$

$$\beta_{\text{seas}}(1) \sim \text{Normal}(\beta_{\text{seas}}(52), \sigma) \quad (\text{S98})$$

593 [SWP: I noticed that I forgot to put a prior on σ so need to re-do this but won't
 594 change the results.] We fix $\alpha(t) = 1$ for all $t < 2020$ and estimate α assuming a
 595 normal prior:

$$\alpha \sim \text{Normal}(1, 0.25). \quad (\text{S99})$$

596 We assume weakly informative priors on ω and τ :

$$\omega \sim \text{Normal}(0, 200) \tau \sim \text{Normal}(104, 26) \quad (\text{S100})$$

597 We assume that the true birth/death rates, population sizes, and recovery rates are
 598 known. We note, however, that assuming $\gamma = 1/\text{week}$ actually correspond to a
 599 mean infectious period of 1.6 weeks, which is much longer than the true value; this
 600 approximation allows us to test whether we can still robustly estimate the intrinsic
 601 resilience given parameters mis-specification. Initial conditions are estimated with
 602 following priors:

$$S(0) = Ns(0) \quad (\text{S101})$$

$$I(0) = Ni(0) \quad (\text{S102})$$

$$s(0) \sim \text{Uniform}(0, 1) \quad (\text{S103})$$

$$i(0) \sim \text{Half-Normal}(0, 0.001) \quad (\text{S104})$$

603 Finally, the Observation model is specified as follows:

$$\text{Cases}(t) \sim \text{Negative-Binomial}(\rho N_{SI}(t), \phi) \quad (\text{S105})$$

$$\rho \sim \text{Half-Normal}(0, 0.02) \quad (\text{S106})$$

$$\phi \sim \text{Half-Normal}(0, 10) \quad (\text{S107})$$

604 where ρ represents the reporting probability and ϕ represents the negative binomial
 605 overdispersion parameter.

606 The model is fitted to four separate time series: (1) incidence time series from
 607 the SIRS model, (2) incidence time series for strain 1 from the two-strain model,
 608 (3) incidence time series for strain 2 from the two-strain model, and (4) combined
 609 incidence time series for strains 1 and 2 from the two-strain model. The model was
 610 fitted using rstan [26, 27]. The resulting posterior distribution was used to calculate
 611 the intrinsic resilience of the seasonally unforced system with the same parameters;
 612 eigenvalues of the discrete-time SIR model were computed by numerically finding
 613 the equilibrium and calculating the Jacobian matrix.

614 **Validations for window-selection criteria**

615 We use stochastic SIRS simulations to validate the window-selection criteria that we
 616 use for the linear regression for estimating empirical resilience. For each simulation,
 617 we begin by generating a random intervention $\alpha(t)$ from random set of parameters.
 618 First, we draw the duration of intervention τ_{np}^* from a uniform distribution between

619 0.5 and 3.5 years. Then, we draw independent normal variables z_i of length $\lfloor 364\tau_{\text{npi}} \rfloor$
 620 with a standard deviation of 0.02 and take a reverse cumulative sum to obtain a
 621 realistic shape for the intervention:

$$x_n = 1 + \sum_{i=n}^{\lfloor 364\tau_{\text{npi}} \rfloor} z_i, \quad n = 1, \dots, \lfloor 364\tau_{\text{npi}} \rfloor. \quad (\text{S108})$$

622 We repeat this random generation process until less than 10% of x_n exceeds 1. Then,
 623 we set any values that are above 1 or below 0 as 1 and 0, respectively. Then, we
 624 randomly draw the minimum transmission during intervention α_{\min} from a uniform
 625 distribution between 0.5 and 0.7 and scale x_n to have a minimum of α_{\min} :

$$x_{\text{scale},n} = \alpha_{\min} + (1 - \alpha_{\min}) \times \frac{x_n - \min x_n}{1 - \min x_n}. \quad (\text{S109})$$

626 This allows us to simulate a realistically shaped interventions:

$$\alpha(t) = \begin{cases} 1 & t < 2020 \\ x_{\text{scale},364(t-2020)} & 2020 \leq t < 2020 + \tau_{\text{npi}} \\ 1 & \tau_{\text{npi}} \leq t \end{cases}. \quad (\text{S110})$$

627 Given this intervention function, we draw \mathcal{R}_0 from a uniform distribution between 1.5
 628 and 3 and the mean duration of immunity $1/\delta$ from a uniform distribution between
 629 0.5 and 2. Then, we simulate the stochastic SIRS model from $S(0) = 10^8/\mathcal{R}_0$ and
 630 $I(0) = 100$ from 1990 to 2025 and truncate the time series to 2014–2025; if the
 631 epidemic becomes extinct before the end of simulation, we discard that simulation
 632 and start over from the intervention generation step. We then apply the window
 633 selection criteria described in the main text to compute the empirical resilience and
 634 compare it against the intrinsic resilience of the seasonally unforced system. We also
 635 compare this with the naive approach that uses the entire distance-from-attractor
 636 time series, starting from the maximum distance. We repeat this procedure 500
 637 times and quantify the correlation between empirical and intrinsic resilience estimates
 638 across two approaches.

Supplementary Figures

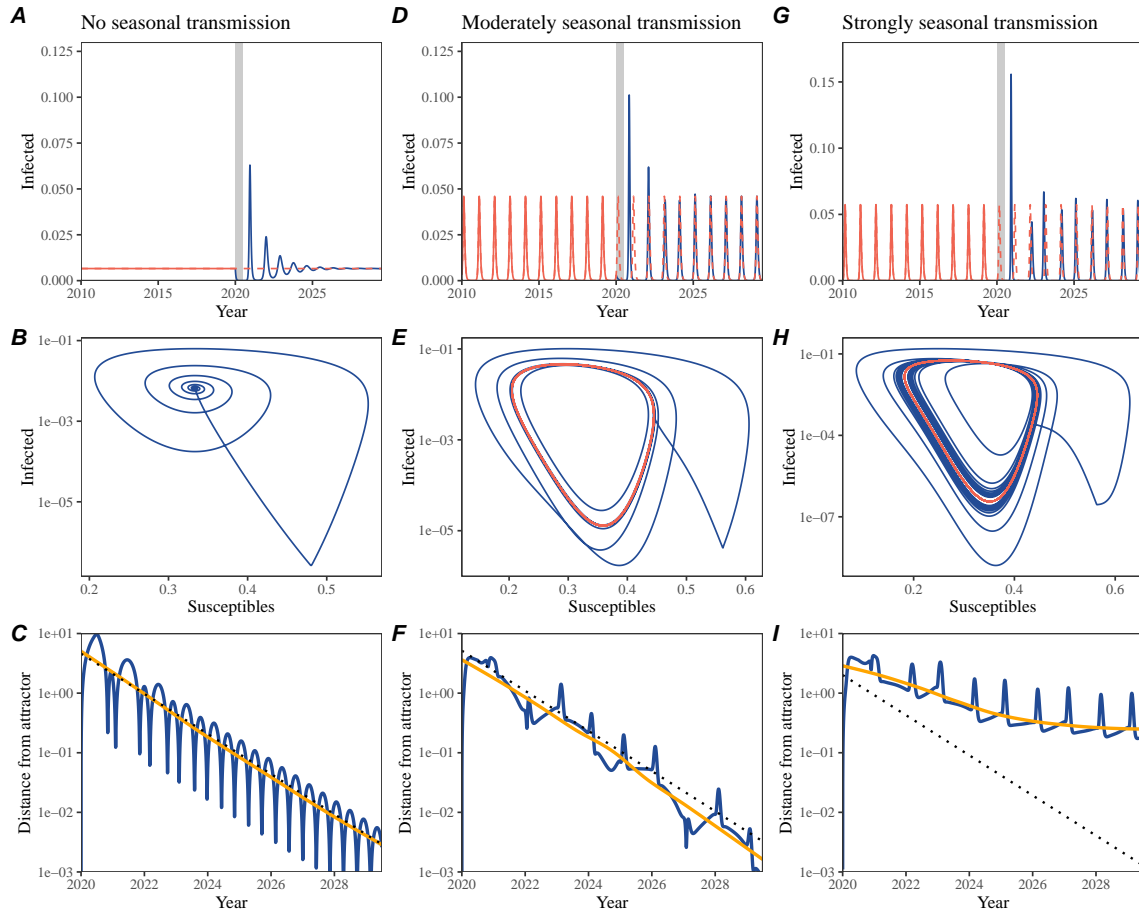


Figure S1: Impact of seasonal transmission on pathogen resilience. (A, D, G) Simulated epidemic trajectories using the SIRS model without seasonal forcing (A), with seasonal forcing of amplitude of 0.2 (D), and with seasonal forcing of amplitude of 0.2 (G). Red and blue solid lines represent epidemic dynamics before and after interventions are introduced, respectively. Red dashed lines represent counterfactual epidemic dynamics in the absence of interventions. Gray regions indicate the duration of interventions. (B, E, H) Phase plane representation of the corresponding model. Red and blue solid lines represent epidemic trajectories on an SI phase plane before and after interventions are introduced, respectively. (C, F, I) Changes in logged distance from attractor over time. Blue lines represent the logged distance from attractor. Orange lines represent the locally estimated scatterplot smoothing (LOESS) fits to the logged distance from attractor. Dotted lines are superimposed as a comparison to have the same slope as the intrinsic resilience of the seasonally unforced system.

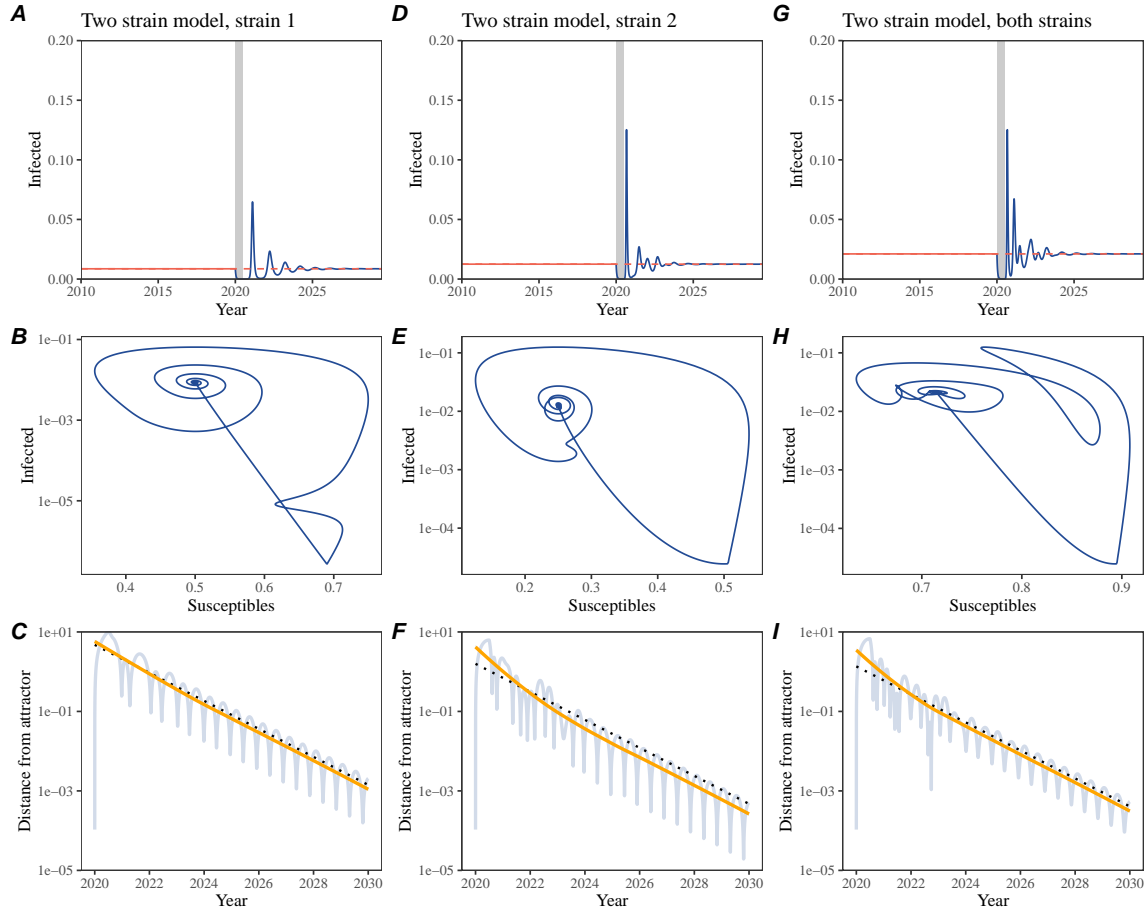


Figure S2: Conceptual framework for measuring pathogen resilience following NPIs for a multi-strain system without seasonal forcing. (A, D, G) Simulated epidemic trajectories using a multi-strain system without seasonal forcing. Red and blue solid lines represent epidemic dynamics before and after interventions are introduced, respectively. Red dashed lines represent counterfactual epidemic dynamics in the absence of interventions. Gray regions indicate the duration of interventions. (B, E, H) Phase plane representation of the corresponding model. Red and blue solid lines represent epidemic trajectories on an SI phase plane before and after interventions are introduced, respectively. (C, F, I) Changes in logged distance from attractor over time. Blue lines represent the logged distance from attractor. Orange lines represent the locally estimated scatterplot smoothing (LOESS) fits to the logged distance from attractor. Dotted lines are superimposed as a comparison to have the same slope as the intrinsic resilience of the seasonally unforced system.

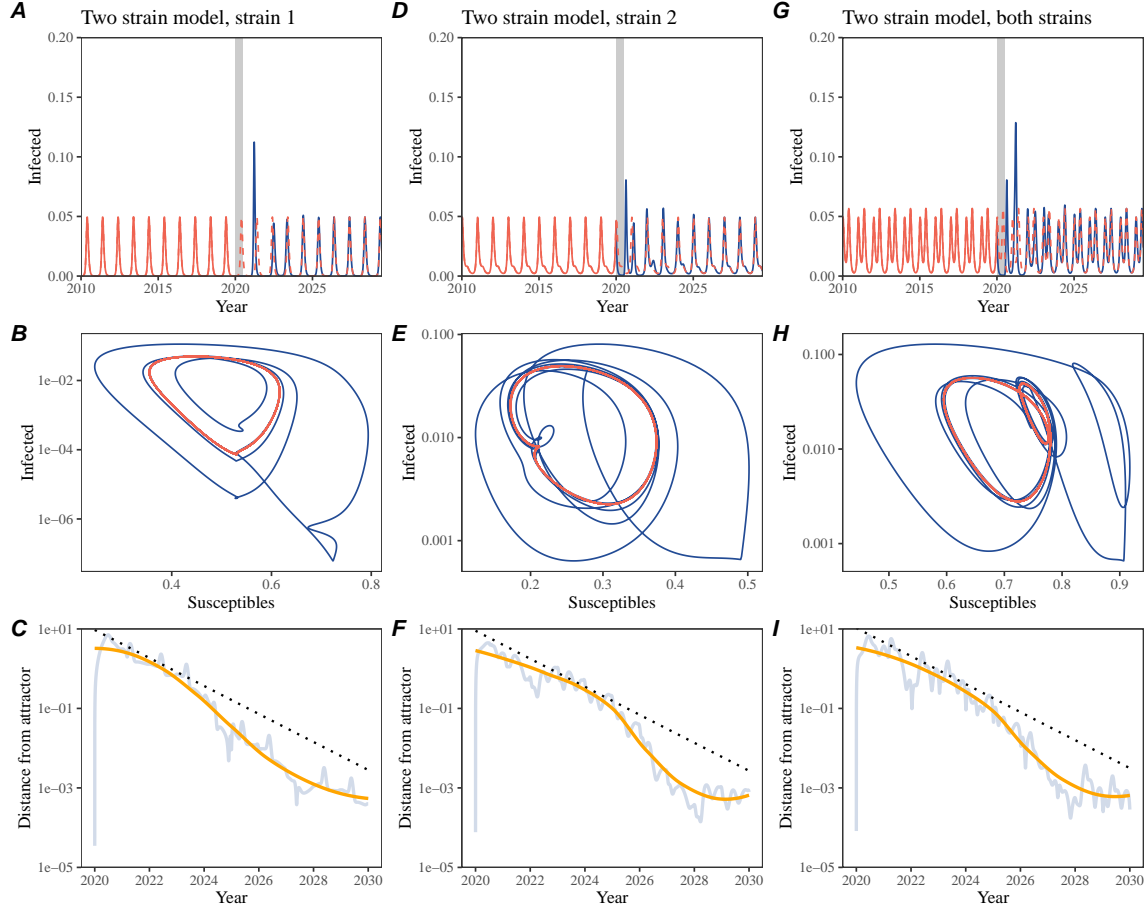


Figure S3: Conceptual framework for measuring pathogen resilience following NPIs for a multi-strain system with seasonal forcing. (A, D, G) Simulated epidemic trajectories using a multi-strain system with seasonal forcing (amplitude of 0.2). Red and blue solid lines represent epidemic dynamics before and after interventions are introduced, respectively. Red dashed lines represent counterfactual epidemic dynamics in the absence of interventions. Gray regions indicate the duration of interventions. (B, E, H) Phase plane representation of the corresponding model. Red and blue solid lines represent epidemic trajectories on an SI phase plane before and after interventions are introduced, respectively. (C, F, I) Changes in logged distance from attractor over time. Blue lines represent the logged distance from attractor. Orange lines represent the locally estimated scatterplot smoothing (LOESS) fits to the logged distance from attractor. Dotted lines are superimposed as a comparison to have the same slope as the intrinsic resilience of the seasonally unforced system.

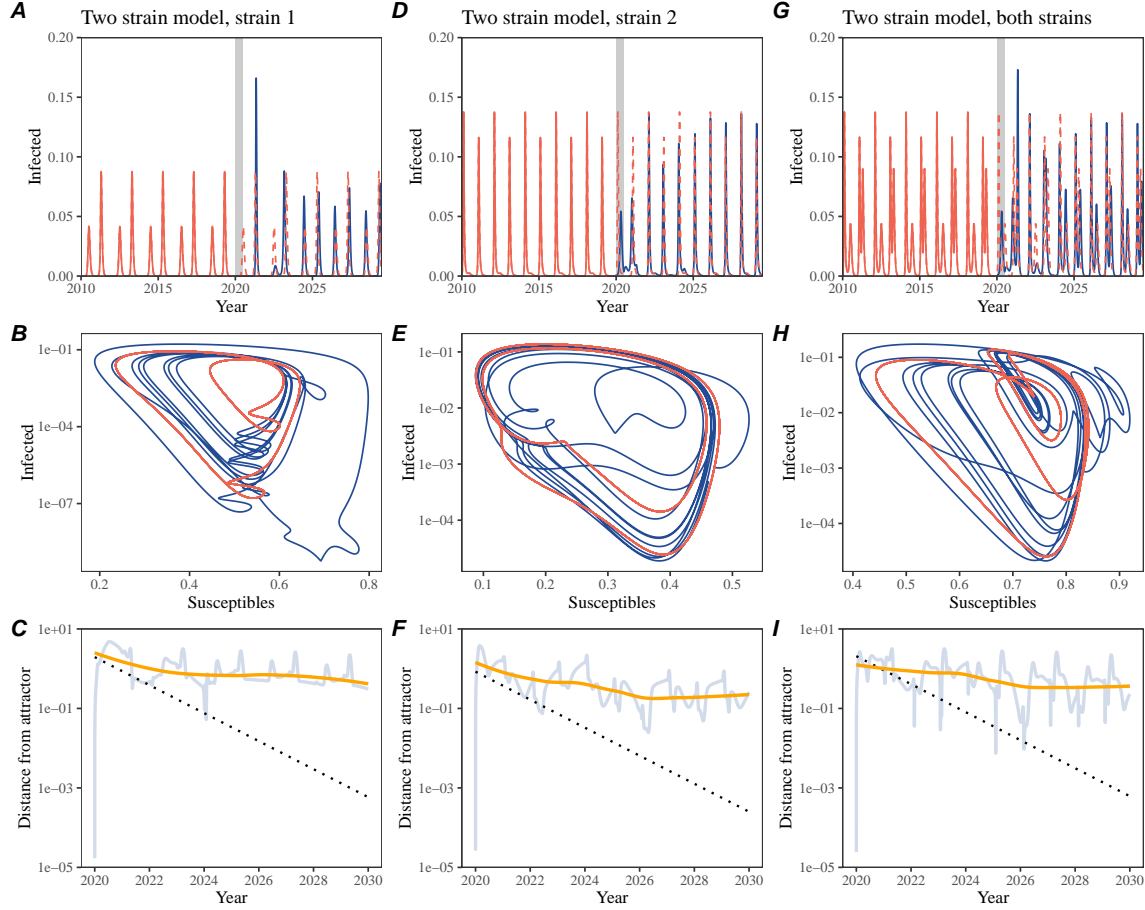


Figure S4: Conceptual framework for measuring pathogen resilience following NPIs for a multi-strain system with strong seasonal forcing. (A, D, G) Simulated epidemic trajectories using a multi-strain system with seasonal forcing (amplitude of 0.4). Red and blue solid lines represent epidemic dynamics before and after interventions are introduced, respectively. Red dashed lines represent counterfactual epidemic dynamics in the absence of interventions. Gray regions indicate the duration of interventions. (B, E, H) Phase plane representation of the corresponding model. Red and blue solid lines represent epidemic trajectories on an SI phase plane before and after interventions are introduced, respectively. (C, F, I) Changes in logged distance from attractor over time. Blue lines represent the logged distance from attractor. Orange lines represent the locally estimated scatterplot smoothing (LOESS) fits to the logged distance from attractor. Dotted lines are superimposed as a comparison to have the same slope as the intrinsic resilience of the seasonally unforced system.

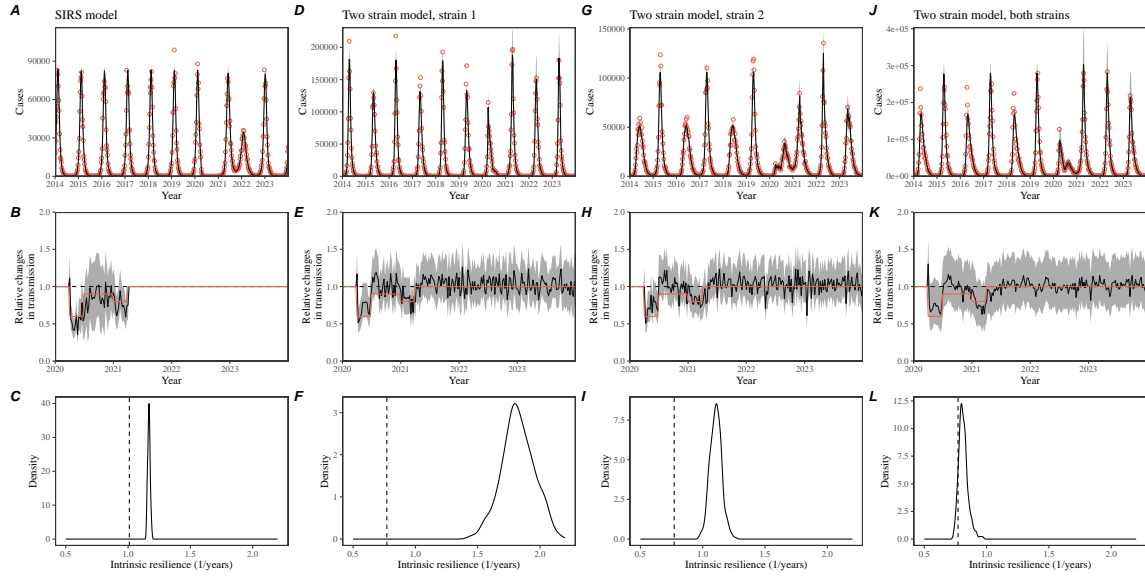


Figure S5: Mechanistic model fits to simulated data and inferred intrinsic resilience. (A, D, G, J) Simulated case time series from corresponding models (red) and SIRS model fits (black). (B, E, H, K) Assumed changes in transmission due to COVID-19 interventions (red) and estimated changes from the SIRS model (black). Solid lines and shaded regions represent fitted posterior median and 95% credible intervals. (C, F, I, L) True intrinsic resilience of the seasonally unforced system (vertical lines) and the posterior distribution of the inferred intrinsic resilience from the SIRS model (density plots).

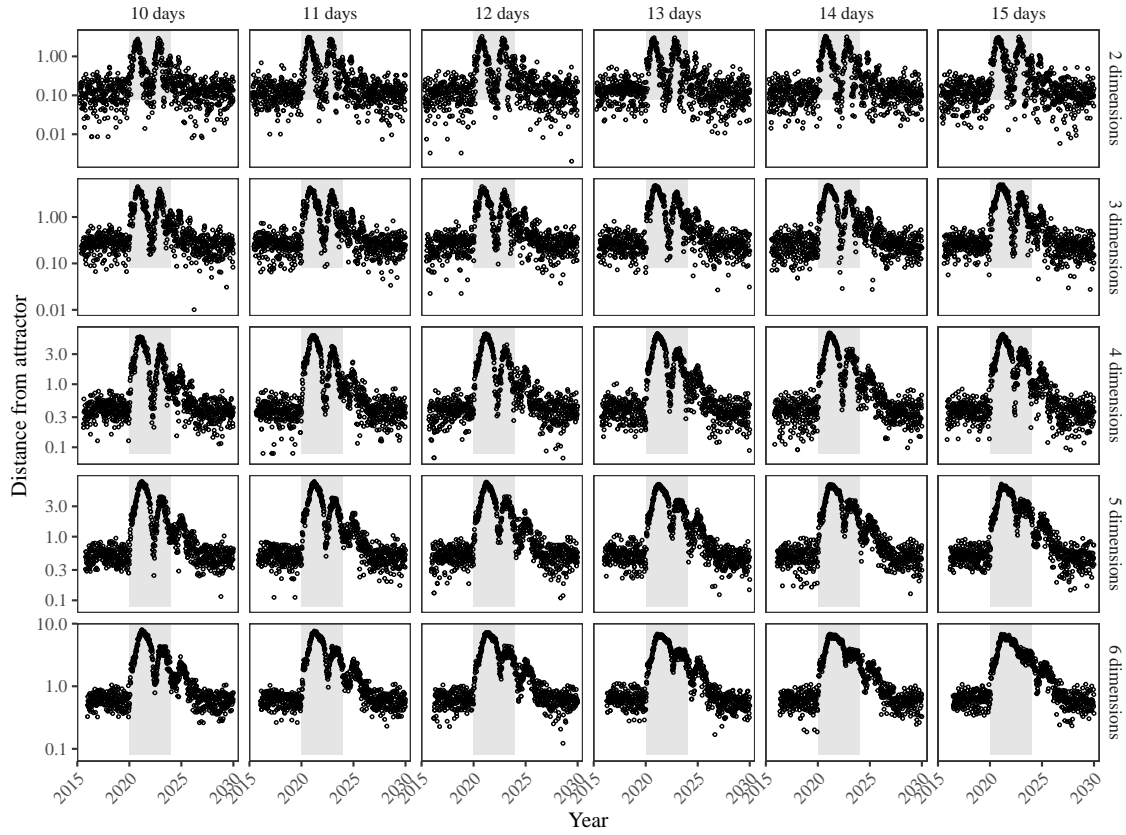


Figure S6: Sensitivity of the distance from attractor to choices about embedding lags and dimensions. Sensitivity analysis for the distance-from-attractor time series shown in Figure 3E in the main text by varying the embedding lag between 10–15 days and embedding dimensions between 2–6 dimensions.

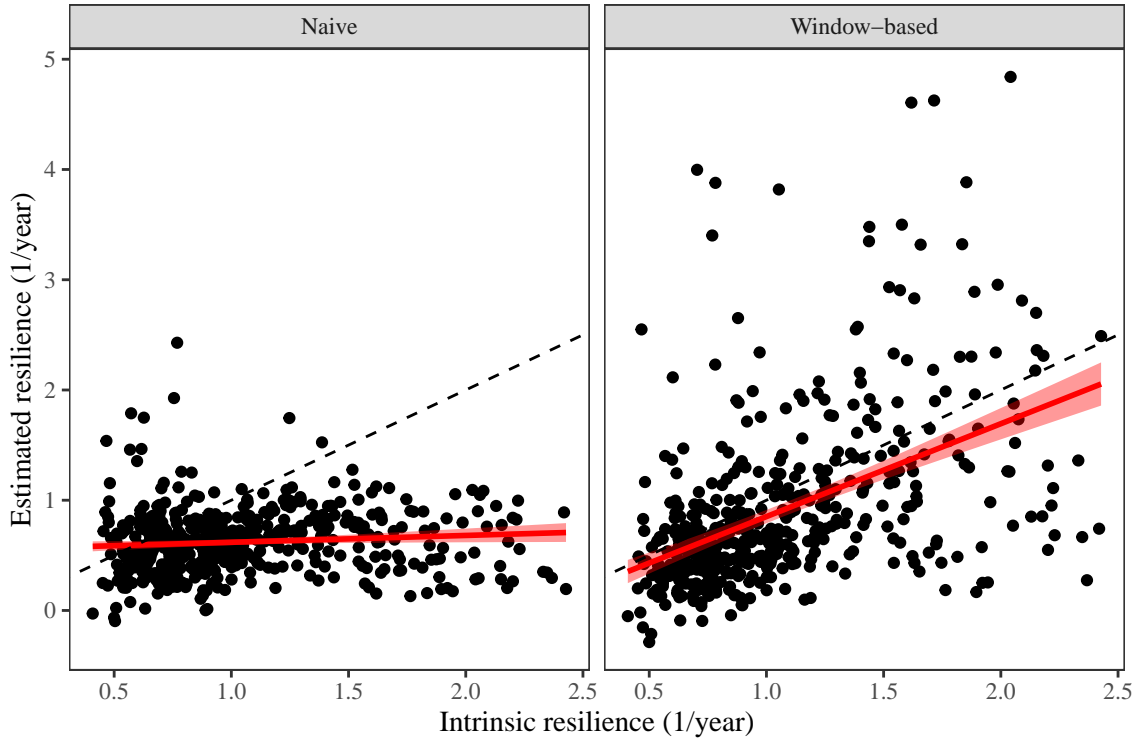


Figure S7: Impact of fitting window selection on the estimation of empirical resilience. We simulate 500 epidemics using stochastic SIRS model with randomly drawn parameters and randomly generated intervention impacts. For each simulation, we reconstruct the empirical attractor based on the approach outlined in Figure 3 and estimate the distance from attractor. The naive approach fits a linear regression on a log scale, starting from the maximum distance until the end of the time series. The window-based approach tries to select an appropriate window by smoothing the distance estimates and finding a time period when the smoothed time series crosses pre-determined threshold, relatively to the maximum distance; then, a linear regression is fitted by using the raw distance within this time period.

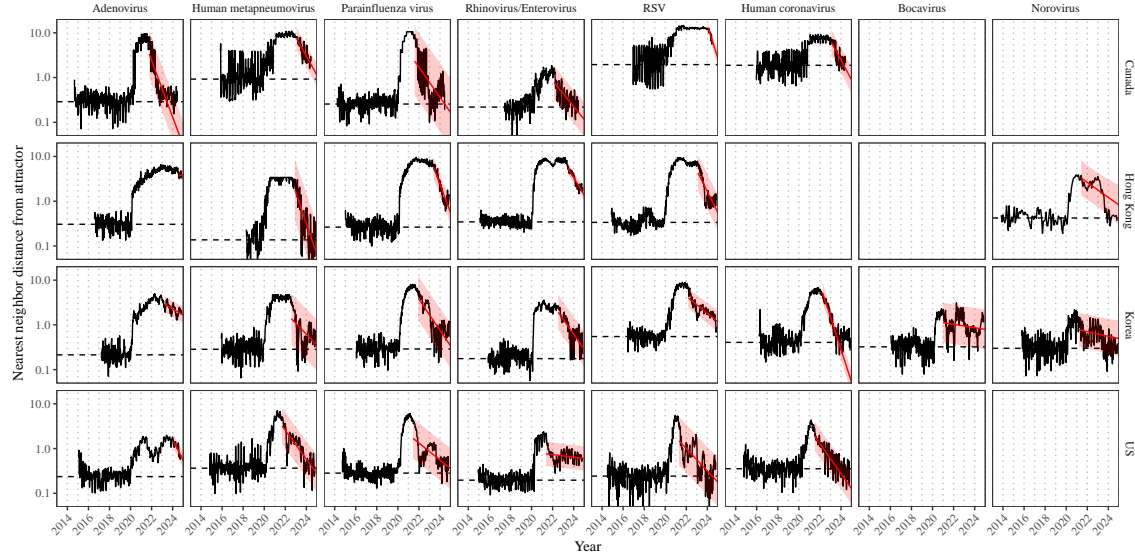


Figure S8: Estimated time series of distance from attractor for each pathogen across Canada, Hong Kong, Korea, and the US. Black lines represent the estimated distance from attractor. Red lines and shaded regions represent the linear regression fits and corresponding 95% confidence intervals. Dashed lines represent the average of the pre-pandemic nearest neighbor distances.

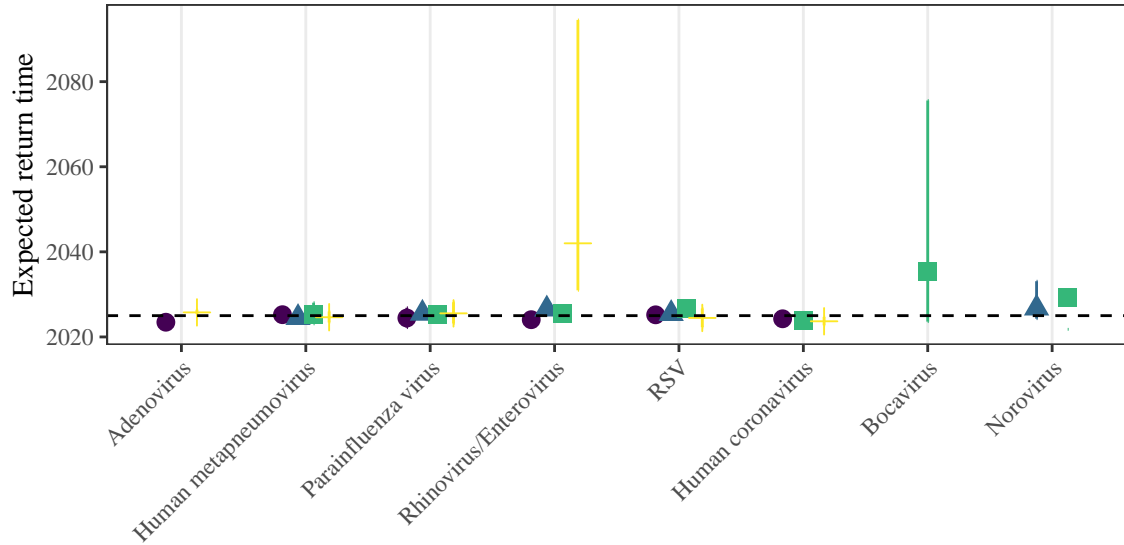


Figure S9: **Predicted timing of when each pathogen will return to their pre-pandemic cycles (zoomed out).** The dashed line in panel B indicates the end of 2024 (current observation time). Error bars represent 95% confidence intervals.

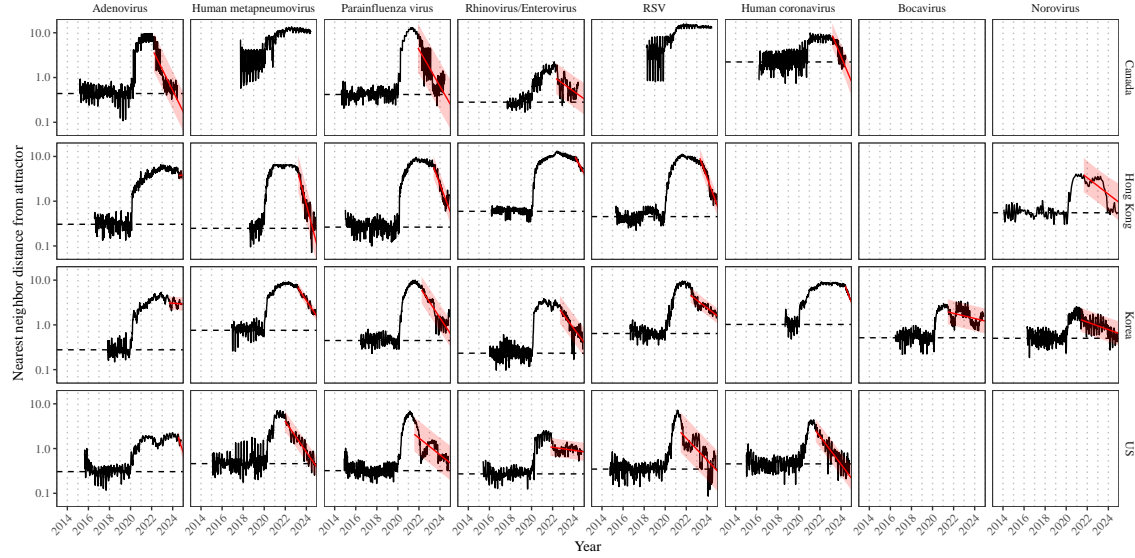


Figure S10: Estimated time series of distance from attractor for each pathogen across Canada, Hong Kong, Korea, and the US using higher embedding dimensions. Black lines represent the estimated distance from attractor. Red lines and shaded regions represent the linear regression fits and corresponding 95% confidence intervals. Dashed lines represent the average of the pre-pandemic nearest neighbor distances. A lower threshold is used for determining embedding dimensions with the false nearest neighbors approach, thereby yielding a higher embedding dimension.

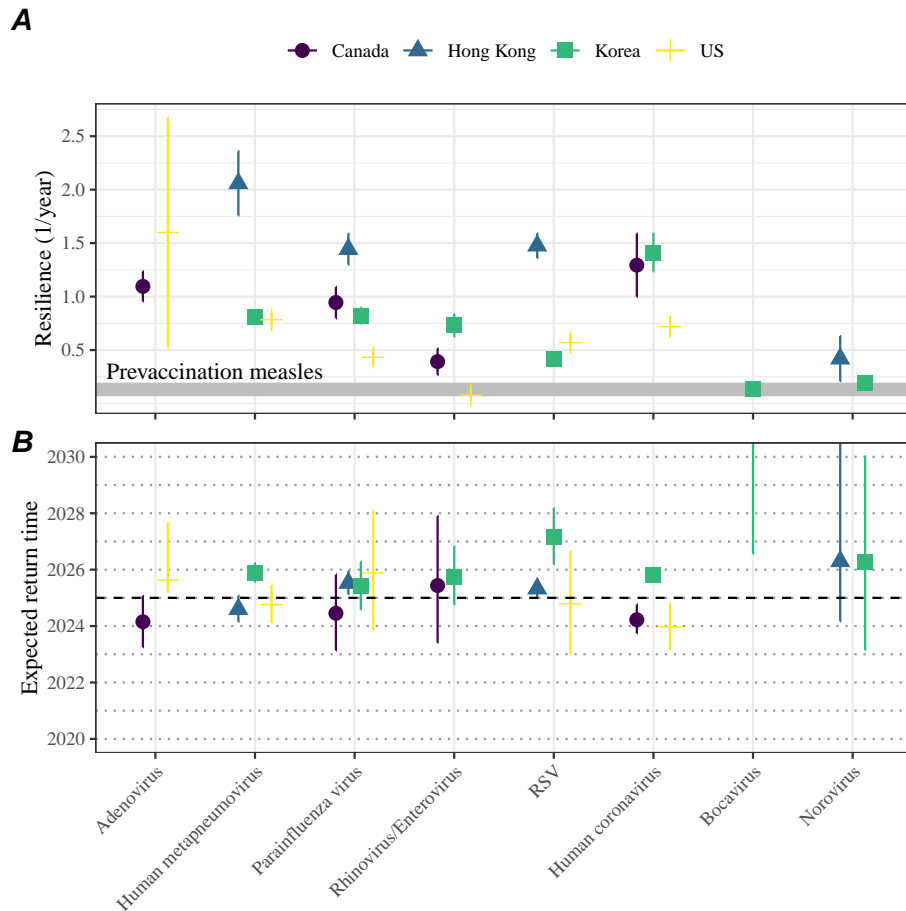


Figure S11: **Summary of resilience estimates using higher embedding dimensions.** (A) Estimated pathogen resilience. The gray horizontal line represents the intrinsic resilience of pre-vaccination measles dynamics. (B) Predicted timing of when each pathogen will return to their pre-pandemic cycles. The dashed line in panel B indicates the end of 2024 (current observation time). Error bars represent 95% confidence intervals. A lower threshold is used for determining embedding dimensions with the false nearest neighbors approach, thereby yielding a higher embedding dimension.

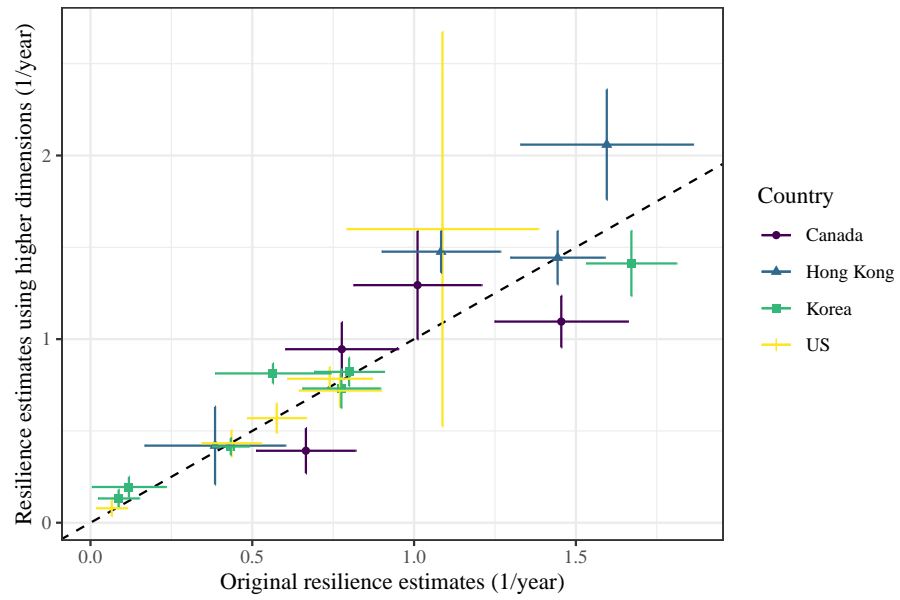


Figure S12: **Comparison of resilience estimates.** Each point represents a resilience estimate for a specific pathogen at a specific country. The x values represent the original resilience estimates presented in Figure 4. The y values represent the original resilience estimates presented in Supplementary Figure S11.

640 References

- 641 [1] Rachel E Baker, Sang Woo Park, Wenchang Yang, Gabriel A Vecchi, C Jessica E
642 Metcalf, and Bryan T Grenfell. The impact of COVID-19 nonpharmaceutical
643 interventions on the future dynamics of endemic infections. *Proceedings of the*
644 *National Academy of Sciences*, 117(48):30547–30553, 2020.
- 645 [2] Gabriela B Gomez, Cedric Mahé, and Sandra S Chaves. Uncertain effects of the
646 pandemic on respiratory viruses. *Science*, 372(6546):1043–1044, 2021.
- 647 [3] Mihaly Koltai, Fabienne Krauer, David Hodgson, Edwin van Leeuwen, Marina
648 Treskova-Schwarzbach, Mark Jit, and Stefan Flasche. Determinants of RSV
649 epidemiology following suppression through pandemic contact restrictions. *Epi-*
650 *demics*, 40:100614, 2022.
- 651 [4] Sang Woo Park, Brooklyn Noble, Emily Howerton, Bjarke F Nielsen, Sarah
652 Lentz, Lilliam Ambroggio, Samuel Dominguez, Kevin Messacar, and Bryan T
653 Grenfell. Predicting the impact of non-pharmaceutical interventions against
654 COVID-19 on *Mycoplasma pneumoniae* in the United States. *Epidemics*,
655 49:100808, 2024.
- 656 [5] Amanda C Perofsky, Chelsea L Hansen, Roy Burstein, Shanda Boyle, Robin
657 Prentice, Cooper Marshall, David Reinhart, Ben Capodanno, Melissa Truong,
658 Kristen Schwabe-Fry, et al. Impacts of human mobility on the citywide trans-
659 mission dynamics of 18 respiratory viruses in pre-and post-COVID-19 pandemic
660 years. *Nature communications*, 15(1):4164, 2024.
- 661 [6] Eric J Chow, Timothy M Uyeki, and Helen Y Chu. The effects of the COVID-19
662 pandemic on community respiratory virus activity. *Nature Reviews Microbiol-*
663 *ogy*, 21(3):195–210, 2023.
- 664 [7] Stephen M Kissler, Christine Tedijanto, Edward Goldstein, Yonatan H Grad,
665 and Marc Lipsitch. Projecting the transmission dynamics of SARS-CoV-2
666 through the postpandemic period. *Science*, 368(6493):860–868, 2020.
- 667 [8] Rachel E Baker, Chadi M Saad-Roy, Sang Woo Park, Jeremy Farrar, C Jessica E
668 Metcalf, and Bryan T Grenfell. Long-term benefits of nonpharmaceutical inter-
669 ventions for endemic infections are shaped by respiratory pathogen dynamics.
670 *Proceedings of the National Academy of Sciences*, 119(49):e2208895119, 2022.
- 671 [9] John-Sebastian Eden, Chisha Sikazwe, Ruopeng Xie, Yi-Mo Deng, Sheena G
672 Sullivan, Alice Michie, Avram Levy, Elena Cutmore, Christopher C Blyth,
673 Philip N Britton, et al. Off-season RSV epidemics in Australia after easing
674 of COVID-19 restrictions. *Nature communications*, 13(1):2884, 2022.
- 675 [10] Stuart L Pimm. The structure of food webs. *Theoretical population biology*,
676 16(2):144–158, 1979.

- 677 [11] Michael G Neubert and Hal Caswell. Alternatives to resilience for measuring
678 the responses of ecological systems to perturbations. *Ecology*, 78(3):653–665,
679 1997.
- 680 [12] Lance H Gunderson. Ecological resilience—in theory and application. *Annual
681 review of ecology and systematics*, 31(1):425–439, 2000.
- 682 [13] Vasilis Dakos and Sonia Kéfi. Ecological resilience: what to measure and how.
683 *Environmental Research Letters*, 17(4):043003, 2022.
- 684 [14] Floris Takens. Detecting strange attractors in turbulence. In *Dynamical Sys-
685 tems and Turbulence, Warwick 1980: proceedings of a symposium held at the
686 University of Warwick 1979/80*, pages 366–381. Springer, 2006.
- 687 [15] Jonathan Dushoff, Joshua B Plotkin, Simon A Levin, and David JD Earn. Dynamical resonance can account for seasonality of influenza epidemics. *Pro-
688 ceedings of the National Academy of Sciences*, 101(48):16915–16916, 2004.
- 690 [16] Alan Hastings, Karen C Abbott, Kim Cuddington, Tessa Francis, Gabriel Gell-
691 ner, Ying-Cheng Lai, Andrew Morozov, Sergei Petrovskii, Katherine Scran-
692 ton, and Mary Lou Zeeman. Transient phenomena in ecology. *Science*,
693 361(6406):eaat6412, 2018.
- 694 [17] Matthew B Kennel, Reggie Brown, and Henry DI Abarbanel. Determining
695 embedding dimension for phase-space reconstruction using a geometrical con-
696 struction. *Physical review A*, 45(6):3403, 1992.
- 697 [18] Eugene Tan, Shannon Algar, Débora Corrêa, Michael Small, Thomas Stemler,
698 and David Walker. Selecting embedding delays: An overview of embedding
699 techniques and a new method using persistent homology. *Chaos: An Interdis-
700 ciplinary Journal of Nonlinear Science*, 33(3), 2023.
- 701 [19] Samit Bhattacharyya, Per H Gesteland, Kent Korgenski, Ottar N Bjørnstad,
702 and Frederick R Adler. Cross-immunity between strains explains the dynamical
703 pattern of paramyxoviruses. *Proceedings of the National Academy of Sciences*,
704 112(43):13396–13400, 2015.
- 705 [20] Bryan T Grenfell, Ottar N Bjørnstad, and Bärbel F Finkenstädt. Dynamics of
706 measles epidemics: scaling noise, determinism, and predictability with the TSIR
707 model. *Ecological monographs*, 72(2):185–202, 2002.
- 708 [21] Virginia E Pitzer, Cécile Viboud, Vladimir J Alonso, Tanya Wilcox, C Jessica
709 Metcalf, Claudia A Steiner, Amber K Haynes, and Bryan T Grenfell. Environ-
710 mental drivers of the spatiotemporal dynamics of respiratory syncytial virus in
711 the United States. *PLoS pathogens*, 11(1):e1004591, 2015.

- 712 [22] Katharine R Dean, Fabienne Krauer, Lars Walløe, Ole Christian Lingjærde, Bar-
713 bara Bramanti, Nils Chr Stenseth, and Boris V Schmid. Human ectoparasites
714 and the spread of plague in Europe during the Second Pandemic. *Proceedings*
715 *of the National Academy of Sciences*, 115(6):1304–1309, 2018.
- 716 [23] Margarita Pons-Salort and Nicholas C Grassly. Serotype-specific immunity
717 explains the incidence of diseases caused by human enteroviruses. *Science*,
718 361(6404):800–803, 2018.
- 719 [24] Sarah Cobey and Edward B Baskerville. Limits to causal inference with state-
720 space reconstruction for infectious disease. *PloS one*, 11(12):e0169050, 2016.
- 721 [25] Edward Goldstein, Sarah Cobey, Saki Takahashi, Joel C Miller, and Marc Lip-
722 sitch. Predicting the epidemic sizes of influenza A/H1N1, A/H3N2, and B: a
723 statistical method. *PLoS medicine*, 8(7):e1001051, 2011.
- 724 [26] Bob Carpenter, Andrew Gelman, Matthew D Hoffman, Daniel Lee, Ben
725 Goodrich, Michael Betancourt, Marcus A Brubaker, Jiqiang Guo, Peter Li,
726 and Allen Riddell. Stan: A probabilistic programming language. *Journal of*
727 *statistical software*, 76, 2017.
- 728 [27] Stan Development Team. RStan: the R interface to Stan, 2024. R package
729 version 2.32.6.